Astronomy & Astrophysics manuscript no. output
February 14, 2026

Asteroseismic forward modelling of 36 β Cep pulsators and inferences on their internal differential rotation

M. Vanrespaille[1], D.J. Fritzewski[1], V. Vanlaer[1], and C. Aerts[1,2,3]

[1] Institute of Astronomy, KU Leuven, Celestijnenlaan 200D, 3001, Leuven, Belgium
e-mail: mathijs.vanrespaille@kuleuven.be
[2] Department of Astrophysics, IMAPP, Radboud University Nijmegen, PO Box 9010, 6500 GL Nijmegen, The Netherlands
[3] Max Planck Institut für Astronomie, Königstuhl 17, 69117 Heidelberg, Germany

ABSTRACT

Context. Asteroseismic observations of the interior rotation of main sequence stars have shown that angular momentum transport is much more efficient than expected. Which transport mechanisms are responsible for this is still unclear. The massive β Cep pulsators are promising stars to constrain these mechanisms as they are the only main sequence pulsators in which radial differential rotation is regularly detected. However, fewer than ten β Cep stars have been asteroseismically modelled in detail so far.
Aims. We aim to expand the sample of asteroseismically forward modelled β Cep pulsators to maximally exploit their potential to observationally constrain angular momentum transport mechanisms. To that end, we seek to constrain their rotation profiles.
Methods. We searched for rotational splitting of non-radial modes in a large β Cep sample with partial mode identifications. These were subjected to a novel forward modelling approach consistently taking second-order rotation effects into account using the state-of-the-art `StORM` oscillation code.
Results. We successfully modelled 36 β Cep stars, constraining their mass, age, rotation frequency, and convective core mass, among other parameters. Herein, second-order rotation effects affect the rotation estimates when exceeding 10% of the critical rotation rate. Like in intermediate-mass main sequence stars, the internal rotation rate globally decreases as the stars evolve along the main sequence. Radial differential rotation is constrained in 17 stars, with the rotation rate in at least 14 of them varying more than 10%. Of these 14 stars, ten have faster inner than outer rotation, while it is the opposite for four stars.
Conclusions. Radial differential rotation strong enough to be clearly detected is common in β Cep stars. Prevailing features in the constrained rotation profiles suggest that β Cep stars typically have a non-monotonic rotation profile.

Key words. Asteroseismology – Stars: oscillations – Stars: massive – Stars: interiors – Stars: evolution – Stars: rotation

1. Introduction

Asteroseismology, the study of pulsating stars, has begun to unveil the interior structure of stars (e.g., Hekker & Christensen-Dalsgaard 2017; García & Ballot 2019; Aerts 2021; Aerts & Tkachenko 2024). Thanks to the recent space photometry revolution brought on by the CoRoT (Auvergne et al. 2009), *Kepler* (Borucki et al. 2010), and TESS (Ricker et al. 2015) telescopes, precise asteroseismic measurements of the interior structure of thousands of stars on and beyond the main sequence are now available (e.g., Kurtz 2022, for a recent observational overview). A key goal of asteroseismology is to unravel transport processes inside the stars, notably angular momentum transport (Talon et al. 1997; Mathis & Zahn 2004, 2005; Rogers et al. 2013). Understanding and calibrating these processes requires a measurement of the internal rotation profile of stars in various evolutionary stages (e.g., Deheuvels et al. 2014; Kurtz et al. 2014; Triana et al. 2015; Di Mauro et al. 2016; Triana et al. 2017; Li et al. 2024; Aerts et al. 2019, for a review).

Asteroseismic studies of hundreds of intermediate-mass main sequence stars with a convective core have revealed that the vast majority of them rotate quasi-rigidly regardless of their age (Li et al. 2020). These observations stand in stark contrast to the predictions of radial differential rotation increasing with age when local conservation of angular momentum applies (Maeder 2009). As such, angular momentum transport in intermediate-mass main sequence stars must be far more efficient than previously thought (Aerts et al. 2019). It is currently unclear which transport mechanisms are responsible for this efficient angular momentum transport along the main sequence, resulting in a systematic uncertainty in stellar evolution models. Moreover, these mechanisms could also transport material, further affecting the star's structure and evolution. Efficient internal mixing could for example refuel the convective core and thus extend the star's lifetime, smoothen chemical gradients, or bring metals produced in the core up to the surface.

Our present study aims to lift our knowledge of the internal rotation properties of high-mass main sequence stars to a population level. The most massive main sequence pulsators are the β Cephei (β Cep) stars. They display low-order p- and g-modes and have masses between 8 and 30 $M_\odot$ (Aerts et al. 2010; Kurtz 2022). Unlike the intermediate-mass main sequence pulsators, a handful of β Cep pulsators with internal rotation measurements display differential rotation, as first reported by Aerts et al. (2003) and summarised by Burssens et al. (2023). Hence, these stars provide valuable constraints to angular momentum transport studies in the high-mass regime. However, the exploitation of this pulsator class is limited by the small number of targets for which the internal rotation rate was measured. Fewer than ten β Cep stars have been asteroseismically modelled in detail and never all together in a consistent population-level study. Of these stars, only five provided constraints on their differential ro-

tation (Burssens et al. 2023). In three stars the rotation rate near the core is up to about 3 times faster than near the surface, while in another star the near-core rotation rate is slightly slower than the envelope's, and the final star rotates quasi-rigidly.

CoRoT observed only one genuine β Cep star but it did not reveal any information on its internal rotation (Degroote et al. 2009) and *Kepler* observed none with proper mode identification. Despite the discovery of hundreds of β Cep stars by TESS (e.g., Shi et al. 2024; Eze & Handler 2024) and other projects (e.g., Labadie-Bartz et al. 2020), only one newly discovered β Cep pulsator, HD 192575, has had its internal rotation profile constrained (Burssens et al. 2023; Vanlaer et al. 2025). This shortage is due to a lack of mode identifications of the detected oscillations, which are necessary to measure the interior rotation rate of β Cep pulsators. The internal rotation is usually measured from rotational splitting of non-radial modes via the Ledoux constant of that splitting (Ledoux 1951). As the low-order modes of β Cep stars do not occur in the asymptotic regimes of low or high frequencies, their Ledoux constants must be extracted from a proper stellar structure model of the star. Such a model is usually found by forward asteroseismic modelling of zonal mode frequencies, whereby the observed frequencies are matched to model predictions. Such forward asteroseismic modelling is only reliable if at least a few observed modes are identified (Ausseloos et al. 2004) and if the first-order treatment of rotation is sufficient, which is seldom the case but most often ignored in the β Cep frequency regime (Suárez et al. 2009).

Mode identification of β Cep pulsations was historically performed from ground-based multi-colour photometry (e.g., Heynderickx et al. 1994) or spectroscopic line profile variations (e.g., Aerts & De Cat 2003). Long-duration multi-site observation campaigns of a few bright β Cep targets gave this research a boost (Handler et al. 2004; Aerts et al. 2004b; Handler et al. 2005; Briquet et al. 2005; Handler et al. 2006, 2012; Briquet et al. 2012). However, these require significant allocations of telescope time, international collaboration efforts and intricate analyses. Consequently, such campaigns are difficult and expensive to scale up to large samples, especially for dim targets. Despite these challenges, modern ground-based multi-site monitoring projects to identify the signals in a few dozen bright β Cep stars are ongoing, such as the Global Asteroseismology Project (Shitrit & Arcavi 2024).

A new avenue towards β Cep mode identification recently opened up in the form of space-based multi-colour photometry. Hey & Aerts (2024) demonstrated that the sparse time series photometry of the *Gaia* space telescope (Gaia Collaboration et al. 2016, 2023) captures the dominant frequency detected by TESS in over 80% of pulsators with an amplitude above 4 mmag. Subsequently, Fritzewski et al. (2025) performed a multi-colour analysis on over 200 β Cep stars based on their amplitudes in the TESS and *Gaia* passbands. For 143 of these stars, they identified the most likely degree of the dominant mode from existing space-based data without requiring additional telescope time. In 33 of these stars, they found rotationally split multiplets including the dominant mode, which were subsequently matched to stellar models to estimate the envelope rotation rate. *Gaia* spectroscopy placed a lower limit on the surface rotation frequency of 20 of these pulsators. Based on these two rotation frequencies, Fritzewski et al. (2025) provided upper limits on the envelope-to-surface rotation ratio of these 20 stars, which varies between 0.3 and 4, albeit with considerable uncertainty.

In this study, we seek to lift β Cep asteroseismology to population level in order to provide observational constraints to future theoretical studies of angular momentum transport in high-mass main sequence stars. To that end, we revisit the sample of Fritzewski et al. (2025) looking for β Cep stars with sufficient mode identifications to asteroseismically model rather than focussing on an individual star as was done so far. This new sample of β Cep stars is described in Sect. 2. Section 3 presents a new grid of stellar models and oscillation predictions, which enables a novel asteroseismic modelling approach consistently including second-order rotation effects described in Sect. 4. Based on these results, Sect. 5 evaluates the impact of the second-order rotation effects while Sect. 6 delves into relations between the asteroseismically inferred rotation and stellar parameters. The detections of differential rotation are shown and discussed in Sect. 7. Finally, a summary and our conclusions are presented in Sect. 8.

2. Target selection

The goal of forward asteroseismic modelling is to constrain a number of free parameters and the input physics of stellar models by matching the observed frequencies of identified modes to those predicted by those models. At minimum, this must constrain the stellar mass and age for a chosen initial metallicity and chemical mixture. For intermediate- and high-mass stars, core-boundary mixing is an essential ingredient (Dupret et al. 2004; Mazumdar et al. 2006; Johnston 2021; Pedersen et al. 2021). We also seek to evaluate the rotation rate and envelope mixing, hence our optimisation problem is five-dimensional. Therefore, we aim for five observational constraints to attempt to break the degeneracies between the free parameters. On top of mode frequencies, two such constraints can be provided by the effective temperature and luminosity. These constraints are now available for most known β Cep stars thanks to the *Gaia* space mission. Since the rotation rate is not known a priori, the azimuthal order of observed modes must be known to account for rotational shifts. Therefore, we require a sample of β Cep stars with at least three observed frequencies with an identified degree and azimuthal order. No sample with these stringent selection requirements on mode identifications has been collected or modelled before.

2.1. Initial input from Fritzewski et al. (2025)

To compose our sample, we started from the 222 β Cep stars presented in Fritzewski et al. (2025). When available, the effective temperature $T_{\rm eff}$ comes from *Gaia*'s ESP-HS pipeline (Fouesneau et al. 2023). In case these were not available, we took the $T_{\rm eff}$ measurement from the GSPPHOT-OB pipeline. Following Fritzewski et al. (2025), we took a conservative relative uncertainty of 10% for $T_{\rm eff}$ as the errors listed in *Gaia* Data Release 3 are unrealistically small (Fouesneau et al. 2023). Together with the measurements of distance, mean G magnitude, and extinction from GSPPHOT-OB these $T_{\rm eff}$ were used to find the luminosity L using Pedersen et al. (2020)'s Model 1 bolometric correction. Finally, like Fritzewski et al. (2025) did, we estimated the surface rotation frequency with an unknown projection factor $f_{\rm rot}\ \sin i$ for 167 β Cep stars by combining the ESP-HS projected surface velocity with the radius computed from L and $T_{\rm eff}$.

We drew on the TESS light curves and Fourier analyses of Fritzewski et al. (2025), using their partial mode identifications as the foundation to build our sample on. By combining *Gaia* and TESS photometry in different passbands, they assigned probabilities to the dominant frequency of each star having a degree l of 0, 1, or 2. For 143 β Cep stars, they could identify a particular degree with a probability greater than 60%. However, the azimuthal orders of these dominant modes are not provided by the multi-passband identification method.

2.2. Further mode identification from rotation splitting

In order to determine the degree and azimuthal order of as many frequencies detected in each target's TESS light curve, we searched for rotationally split multiplets. For the low-order modes of single non-magnetic β Cep stars, these multiplets show up as series of up to $2l + 1$ roughly evenly spaced frequencies in the Fourier transform of a light curve.

Specifically, we sought multiplets that satisfy at least four of these five conditions: a) the probability of the degree suggested by any rotational splitting is at least 40% in Fritzewski et al. (2025); b) all frequencies in the multiplet were detected; c) the dimensionless asymmetry, defined as $A_{|m|} = \frac{2f_0 - f_m - f - m}{f_m + f - m}$ with f_m the multiplet's frequency of azimuthal order m (Guo et al. 2024), lies within $\pm$ 10%; d) the mean splitting within the multiplet is smaller than 0.75 d^{-1}; and e) if available, the mean splitting is compatible with the $f_{\rm rot} \sin i$ measurement from *Gaia* and is less than a factor 2 different from any other identified multiplet's mean splitting. If a target features a candidate for a rotationally split multiplet and another high-amplitude signal with no similar splitting around it, we considered that signal to be due to a radial mode. If Fritzewski et al. (2025) assigns that signal to a radial mode with a probability over 60%, we dropped condition a) from the candidate for a rotationally split multiplet. Based on these stringent conditions, we found 38 stars with at least three identified modes from two or more multiplets or radial modes, with at least two modes belonging to the same multiplet.

2.3. Literature pulsators

To validate our mode identifications and the novel asteroseismic forward modelling strategy described in Sect. 4, we seek β Cep stars with forward modelling in the literature to compare to. One such well-known target, 12 Lac (Handler et al. 2006; Dziembowski & Pamyatnykh 2008; Desmet et al. 2009), is already included in the sample of Fritzewski et al. (2025). We used this pulsator to test our mode identification, although its value to testing our forward modelling is limited as key stellar parameters such as its mass are only weakly constrained because the strength of its core-boundary mixing is unclear (Desmet et al. 2009). In terms of mode identification, Fritzewski et al. (2025) finds the same result for the dominant mode degree as Handler et al. (2006) and Desmet et al. (2009). For this star, we used the degree and azimuthal order identifications of the other modes from Desmet et al. (2009), expanded with a new frequency detected in the TESS light curve. Another known β Cep star already in the sample of Fritzewski et al. (2025) is KZ Mus. It has not been modelled before and is thus not useful to test our modelling, though we can verify the mode identifications with those of Handler et al. (2003) and Shobbrook et al. (2006).

As 12 Lac's stellar parameters are weakly constrained, we require other β Cep stars with detailed modelling results in the literature. For that reason and to further expand our sample, we added five previously modelled β Cep stars with unambiguously identified modes. These are HD 129929 (Aerts et al. 2003, 2004b; Dupret et al. 2004), ν Eri (Aerts et al. 2004a; Ausseloos et al. 2004; De Ridder et al. 2004; Pamyatnykh et al. 2004; Jerzykiewicz et al. 2005; Dziembowski & Pamyatnykh 2008; Suárez et al. 2009), β CMa (Handler et al. 2003; Desmet et al. 2006; Mazumdar et al. 2006; Shobbrook et al. 2006), θ Oph (Handler et al. 2005; Briquet et al. 2005, 2007), and HD 192575 (Burssens et al. 2023; Vanlaer et al. 2025; Vandersnickt et al. submitted). For these stars, we took the $T_{\rm eff}$, L, frequencies, and identifications of l and, if available, m reported in the literature.

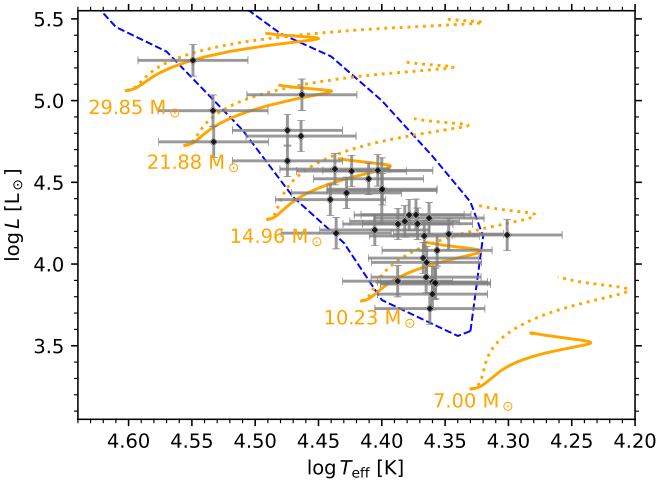

Fig. 1: Hertzsprung-Russell diagram with the targets in our sample. The p-mode instability strip of Burssens et al. (2020) is indicated by the dashed blue line. Some examples of evolutionary tracks of our model grid are shown in orange, with solid lines indicating the models with the weakest core overshoot and envelope mixing and dotted lines those with the strongest mixing.

While additional β Cep stars are available in the literature, we excluded them from this study. β Cep itself, the archetype of this class of pulsators, was not included in our sample as its frequency splitting is interpreted as due to a magnetic field rather than rotational effects (Telting et al. 1997; Shibahashi & Aerts 2000). Another well-known β Cep pulsator we excluded is V2052 Oph (Handler et al. 2012; Briquet et al. 2012) as its rotationally split mode likely has degree $l = 4$, while we focus on pulsation modes with $l = 0, 1, 2$. For similar reasons, we rule out β Cru (Cotton et al. 2022). Next, the CoRoT target HD 180642 (Degroote et al. 2009; Briquet et al. 2009) was excluded as its dominant high-amplitude radial mode is highly non-linear, while the identifications of its low-amplitude modes are unclear. Finally, 16 Lac (Thoul et al. 2003) and δ Cet (Aerts et al. 2006) lack a clear rotationally split multiplet as the former has no two signals of the same l while the latter's m are unclear.

Our work presents the largest sample of β Cep stars with sufficient identified modes of $l = 0, 1, 2$ to perform asteroseismic forward modelling in a homogeneous way, summarised in Table D.1. Of the 36 stars we successfully model in Sect. 4, 24 have an identified radial mode, while 17 have more than one identified rotationally split multiplet. Figure 1 shows the distribution of our targets in the Hertzsprung-Russell diagram (HRD) alongside some evolutionary tracks.

3. Grid of stellar models

Asteroseismic forward modelling requires stellar models with predictions of the possible pulsation frequencies to match the observations to. Herein, one can either use a model grid with medium resolution or create an initial grid with poor resolution and continually refine the grid resolution around each star's optimal position in the parameter space, as done by past studies that modelled an individual β Cep star (e.g. Dupret et al. 2004; Briquet et al. 2007; Suárez et al. 2009; Burssens et al. 2023). Since we seek to model a large number of pulsators, refining the grid for each star is not feasible. As Fig. 1 shows, our stars are spread over a broad area of the HRD, so we require a grid covering the

Table 1: Parameter space of our MESA-StORM grid.

parameter	min.	max.	number
M [$M_\odot$]	7.00	29.85	43
$\log D_{\rm mix,0}$ [cm^2 s^{-1}]	1.0 ; 2.0	5.0 ; 6.0	5
$f_{\rm ov}$	0.005	0.035	7
$X_{\rm c}$	0.0001	0.701	118
$f_{\rm rot}/f_{\rm crit}$	0.0	0.40	41

entire β Cep instability strip, which was not yet available in the literature. Therefore, we computed a new grid of stellar models and computation predictions, described here.

3.1. Models of stellar structure and evolution

We computed a new stellar model grid using the stellar structure and evolution code Modules for Experiments in Stellar Astrophysics (MESA) version r24.08.1 (Paxton et al. 2011, 2013, 2015, 2018, 2019; Jermyn et al. 2023). These models were optimised for asteroseismic modelling by ensuring improved spatial resolution around burning and convective regions while still being efficient enough to compute a large grid. The models contain the solar metal fractional abundances from Asplund et al. (2009). We used the corresponding radiative opacity grids of the Opacity Project library (Seaton 2005), except at low temperatures where they are blended with the opacity tables of Ferguson et al. (2005). The equation of state is a blend of FreeEOS (Irwin 2004) and Skye (Jermyn et al. 2021). Our custom nuclear network contains 32 isotopes covering the four cold CNO-cycles and the α-backbone up to ^{56}Fe and ^{56}Ni. We exclusively used the nuclear rates of the JINA REACLIB (Cyburt et al. 2010).

We used the Ledoux criterion for convection. As high-mass main sequence stars have no convective envelope, they are only weakly sensitive to the mixing-length parameter $\alpha_{\rm MLT}$, which was set to 2.0. Since we lack strong observational constraints on the metallicity from high-resolution spectroscopy for most of our stars, we fixed the initial metallicity Z at 0.014. We included the levels of core-boundary and envelope mixing as free parameters in the models. Core-boundary mixing was implemented as exponential overshooting. Expressed in units of the local pressure scale height H_p, the core overshoot parameter $f_{\rm ov}$ varies from 0.005 to 0.035 in steps of 0.005, where the overshooting begins a distance of $0.005\,H_p$ into the convective core. Beyond the overshooting zone, the mixing profile is given by $D_{\rm mix} = D_{\rm mix,0}\frac{\rho_0}{\rho}$, with ρ the local density and ρ_0 the density at the base of the envelope, to represent envelope mixing by internal gravity waves instead of classical rotational mixing (Rogers & McElwaine 2017). For models with $M < 13\,M_\odot$, $D_{\rm mix,0}$ varies from 10 to 10^5 cm^2 s^{-1} in logarithmic steps $\Delta \log D_{\rm mix,0} = 1$. This upper limit is set by the requirement to avoid fully mixed models, while the lower limit is set so the structure profiles are still significantly altered as some level of envelope mixing is necessary to explain asteroseismic observations in intermediate- and high-mass main sequence pulsators (Moravveji et al. 2015; Rehm et al. 2024). For the same reasons, $D_{\rm mix,0}$ ranges from 10^2 to 10^6 cm^2 s^{-1} for models with an initial mass $M > 13\,M_\odot$.

To sample the entire β Cep space, we computed main sequence models with 43 values for M between 7 and 30 $M_\odot$ in logarithmic steps of $\Delta \log M = 0.015$. This results in typical steps in M of 0.5 $M_\odot$ with tighter sampling around lower M where the model's position on the HRD is more sensitive to M. Each MESA run created output at 118 values of central hydrogen fraction $X_{\rm c}$ between 0.701 and 0.0001, with the resolution increasing as $X_{\rm c}$ decreases. This fine age resolution and mass coverage are necessary to ensure there is a model reasonably close to the star's true parameters. Table 1 summarises the parameter space and output frequency of our grid.

3.2. Oscillation computations

To predict the pulsation frequencies of the $l = 0, 1, 2$ modes, we employed the adiabatic oscillation code Stellar Oscillations with Rotation (StORM, Vanlaer et al. submitted, https://storm.stellar-oscillations.org/). It is optimised for the low-order modes of β Cep stars and includes the second-order rotation effects due to the Coriolis force and rotational deformation. The latter is approximated by the Chandrasekhar-Milne expansion to second-order (Chandrasekhar 1933; Tassoul 1978) applied to an undeformed stellar input model. This deformation increases the star's total size and hence reduces all mode frequencies, albeit by different amounts. Moreover, coupling between spherical harmonics, including toroidal components, further perturbs the oscillation frequencies from those in a spherically symmetric equilibrium model (Saio 1981; Lee & Baraffe 1995). As frequencies with a different azimuthal order m are perturbed at different levels, these second-order effects of rotation produce asymmetrically rotationally split multiplets.

Recently, Mombarg et al. (2025) compared 2D computations of stellar models and their pulsations to StORM which showed the frequencies and rotational asymmetries to be sufficiently accurate for practical asteroseismic modelling of β Cep pulsators. Consequently, we can include the observed rotational splitting in non-radial modes as additional constraints in the asteroseismic forward modelling alongside the identified zonal mode frequencies used in β Cep modelling in the past. This strongly constrains the rotation rate $f_{\rm rot}$ in particular, letting us include $f_{\rm rot}$ as a fifth free parameter in our forward modelling. We computed the oscillations at $f_{\rm rot}$ from zero up to 40% of the Keplerian critical rotation rate $f_{\rm crit}$ in steps of $1\%\,f_{\rm crit}$. Although β Cep stars are known to feature differential rotation, we assumed rigid rotation in our oscillation computations because the rotation profiles of β Cep stars are not known a priori. Additionally, this limits the dimensionality of our modelling problem while still accounting for the effects of rotation in a more advanced way than any forward modelling of an entire sample of β Cep stars in the literature. We scanned for frequencies with degrees $l = 0, 1, 2$ between 2 and 15 d^{-1}, which consistently includes the radial orders $n_{\rm pg}$ from -3 to +5. Herein StORM defines $n_{\rm pg}$ using the Eckart-Scuflaire-Osaki scheme (Eckart 1961; Scuflaire 1974; Osaki 1975), except for $l = 1$ modes which use the Takata scheme (Takata 2006).

4. Asteroseismic modelling strategy

Our modelling approach is inspired by that of Ausseloos et al. (2004), who modelled the β Cep variable ν Eri by first fitting the identified fundamental radial mode to find the stellar age. This helps to reduce the dimensions of the fitting problem, thus lowering the computation time, which is of great importance when modelling an entire sample. In this work, we generalised this methodology to consistently optimise $f_{\rm rot}$ alongside the other free parameters rather than estimating $f_{\rm rot}$ in an a posteriori step as was done in past β Cep studies. Herein we make use of the measurements of $T_{\rm eff}$ and L available in the *Gaia* era. We found this new methodology to also work well for stars without an identified radial mode. First, we describe our methodology in detail and test it on the validation stars.

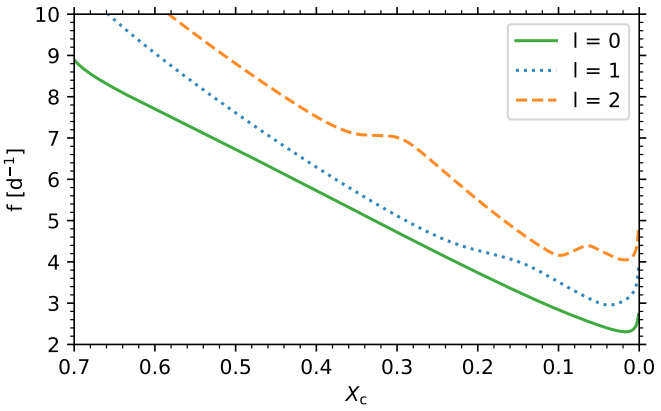

Fig. 2: Evolution of the radial (green solid line), dipole (blue dotted line) and quadrupole (orange dashed line) zonal p_1-modes against the central hydrogen mass fraction as a proxy for main sequence age of a non-rotating $\sim$15 $M_\odot$ star.

4.1. Method for stars with an identified radial mode

Following Ausseloos et al. (2004) and Desmet et al. (2006), we first fitted the frequency of the radial mode, which we refer to as the 'fixed mode', to fix the age along each MESA evolutionary track in the grid. Figure 2 shows how the fundamental radial mode frequency decreases monotonically along such a track until it approaches the TAMS because its frequency is dependent on the mean stellar density, which decreases across the main sequence as the stellar radius increases. Subsequently, we sought the age where the predicted radial mode frequency matches the observed frequency. Then we performed a cubic interpolation of all predicted frequencies and stellar parameters to that age such that the observed radial mode frequency is reproduced exactly.

The model age also depend on $f_{\rm rot}$ because rotationally induced deformation and mode coupling alters the predicted radial mode frequency. Therefore, we need to find the optimal $f_{\rm rot}$ for that evolutionary track. To do so, we used the observed rotational splitting $f_{\rm obs}$ in identified non-radial modes. For each $\Delta f_{\rm rot}$ in the grid, we repeated the procedure of fixing the age and interpolating. In these age-interpolated models, we compared the predicted rotational splitting $\Delta f_{\rm pred}$ with $\Delta f_{\rm obs}$ by calculating $\chi^2_{\rm split} \equiv \sum_j (\Delta f_{{\rm pred},j} - \Delta f_{{\rm obs},j})^2 / \sigma^2_{\Delta f,j}$ where j iterates over each identified non-zonal mode. For $\Delta f_{\rm pred}$, we took the splitting of the multiplet of matching l with a zonal frequency closest to the observed zonal frequency. Herein, we considered modes with $n_{\rm pg}$ between -3 and +5. No identified mode was ultimately matched to $n_{\rm pg} = -3$ or $n_{\rm pg} = +5$, indicating this range in $n_{\rm pg}$ is sufficiently broad. We subsequently sought the $f_{\rm rot}$ that optimally reproduces the observed splitting as the minimum of a cubic interpolation of $\chi^2_{\rm split}$. Finally, we linearly interpolated all predicted frequencies and stellar parameters to that optimal $f_{\rm rot}$.

Our interpolation in age and then rotation rate effectively reduces an entire evolutionary track of 118 models with pulsation predictions at 41 rotation rates to one model with an optimal age and rotation rate. This procedure was performed for all 1505 evolutionary tracks in our grid. For each optimised model, we evaluated the reduced χ^2 cost function including $\log T_{\rm eff}$, $\log L$, the identified zonal frequencies and $\Delta f_{\rm obs}$ in identified multiplets. Following Aerts et al. (2018), we then performed statistical model selection and parameter estimation by taking the $\exp(-\chi^2/2)$ weighted average over the optimised stellar models situated in the observed 2σ error ellipse in the HRD. The uncertainty on the parameters is provided by the weighted standard deviation. However, due to the tiny observational uncertainty on the mode frequencies, any minor difference in predicted frequency between stellar models produces a large difference in χ^2. Consequently, the statistical model is almost always dominated by one stellar model, leading to the uncertainty on stellar parameters being very small.

Unknown systematic uncertainties are induced by setting the input physics in the stellar models. Aerts et al. (2018) examined the zonal mode frequencies for SPB and β Cep stars between MESA models employing a variety of different input physics. For the low-order modes in β Cep stars, the largest frequency changes are on the order of 10^{-2} d^{-1}. However, because we fix one frequency first, our modelling procedure is primarily sensitive to the differences between frequencies while the systematic error estimates reported by Aerts et al. (2018) usually shift the mode frequencies by a similar value. Therefore, we used 10^{-3} d^{-1} as the theoretical uncertainty on the frequencies. The observational frequency errors of the dominant identified modes are typically two orders of magnitude smaller than these systematic uncertainties. Consequently, the observational uncertainties can be ignored in practice, a well-known phenomenon in asteroseismology of intermediate- and high-mass stars (Briquet et al. 2007; Desmet et al. 2009). Despite the inflated frequency uncertainty, there were still targets for which one model dominated the statistical model, resulting in underestimated uncertainties of stellar parameters. To circumvent this, we set the minimal uncertainty of M, $\log D_{\rm mix,0}$, and $f_{\rm ov}$ to half the grid step and propagated these uncertainties to all other evaluated parameters.

In the methodology described above, it was implicitly assumed that the radial order of the fixed mode was known, which is not the case. Therefore, we repeated the procedure thrice, trying $n_{\rm pg} = 1, 2, 3$ for the fixed mode. We examined the results of these three runs and manually selected the most likely identification of the radial order based on three factors. From most to least important, they are 1) whether the model featured predicted frequencies that can explain any observed unidentified mode signals; 2) the reduced χ^2 value; 3) the model's proximity to the observed position in the HRD. Once the $n_{\rm pg}$ of the fixed mode is settled, the $n_{\rm pg}$ of the other identified modes become immediately clear.

4.2. Method for stars with only identified non-radial modes

For those targets that have an identified radial mode, we prioritised fixing their frequency. However, 12 stars have two or more rotationally split multiplets, but no identified radial mode. For these stars, we thus had to use a non-radial zonal mode as the fixed mode. As Fig. 2 shows, the frequencies of zonal non-radial modes decrease similarly to those of the radial modes at most ages. However, they can evolve non-monotonically. Consequently, the age cannot always be uniquely fixed from non-radial zonal modes. As increases in frequency with age occur more commonly at lower frequencies we picked the identified zonal mode with the highest frequency as the fixed mode to avoid this non-monotonic behaviour as much as possible.

When selecting the radial order of that fixed mode, we also considered $n_{\rm pg} = -2$, $n_{\rm pg} = -1$ and, if the fixed mode has $l = 2$, $n_{\rm pg} = 0$ on top of $n_{\rm pg} = 1, 2, 3$. Afterwards we inspected the fixed ages of the interpolated models within the 2σ uncertainty ellipse in the HRD to ensure they were unaffected by non-monotonicity. Only one star was affected and was consequently excluded from our sample of successfully modelled β Cep stars.

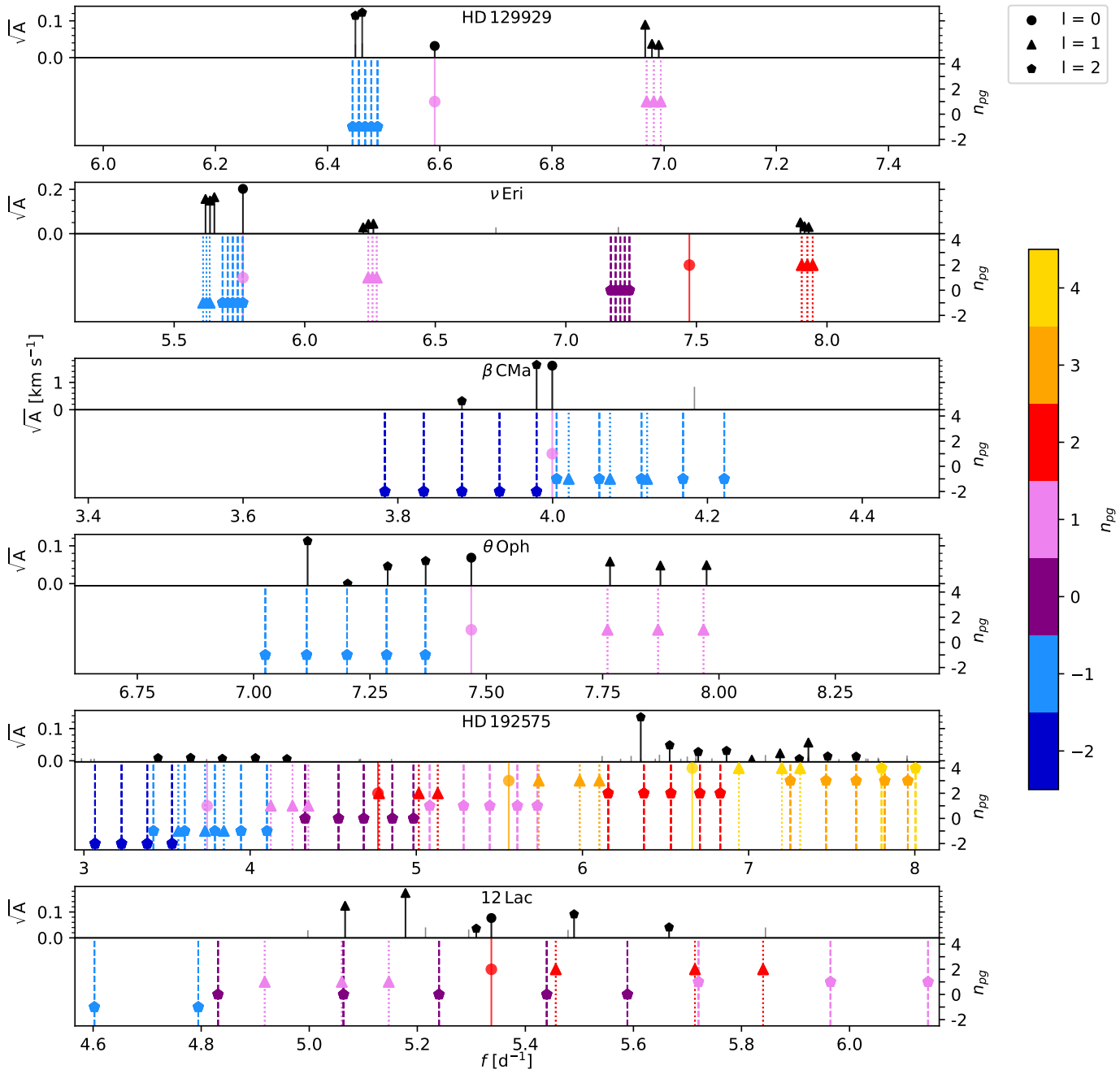

Fig. 3: Comparing the observed (top) and best model's frequencies (bottom) for the six validation stars. The x-axis is different for each star. The y-axis in the top panel shows the square root of the relative flux amplitude (except in β CMa, whose spectroscopically detected signals are given in km s^{-1}). Unidentified signals are grey lines while identified ones are black and topped with a marker indicating the degree as a circle for radial modes, triangle for dipole modes, and pentagon for quadrupole modes. In the bottom panel, the colours and y-axis indicate the radial order.

4.3. Validation of the procedure

To test the reliability of our novel modelling strategy, we examined the validation targets described in Sect. 2.3, including 12 Lac. Figure 3 compares the observed signals and the frequencies predicted in the best model. The zonal frequency of most multiplets closely matches the observed one, with the $l = 2$ multiplet in 12 Lac being a notable exception because it is strongly coupled to the radial mode. While most rotational splitting is reproduced reasonably well, the splitting is overestimated in some multiplets and underestimated in others, particularly in HD 192575, which may indicate strong differential rotation. Moreover, the $(n_{\rm pg}, l) = (-1, 2)$ zonal frequency of HD 192575's best model is 0.04 d^{-1} smaller than observed. Recently, Vandersnickt et al. (submitted) discovered that this multiplet is affected by an internal magnetic field. They predict that this magnetic field increases the frequencies of this multiplet on the order of magnitude of 0.1 d^{-1}, explaining the discrepancy.

Table 2 shows the results of our modelling and the best models reported in the literature, including the metallicity Z used in the literature modelling. Overall, there is a good agreement for

Table 2: Comparison of the parameter estimates from our forward modelling to modelling results reported in the literature.

	Our statistical model						Model(s) in literature							
star	M [$M_\odot$]	$\log T_{\rm eff}$ [K]	$\log L$ [$L_\odot$]	$\log g$ [cm s^{-2}]	$X_{\rm c}$	$f_{\rm rot}$ [d^{-1}]	M [$M_\odot$]	$\log T_{\rm eff}$ [K]	$\log L$ [$L_\odot$]	$\log g$ [cm s^{-2}]	$X_{\rm c}$	$f_{\rm rot}$ [d^{-1}]	Z	Ref.
HD 129929	8.91	4.342	3.817	3.892	0.318	0.0132	9.35	4.350	3.857	3.905	0.353	0.0127 - 0.0147	0.0188	(1)
ν Eri	8.61	4.321	3.809	3.803	0.267	0.0265	7.83	4.306	3.720	3.789	...	...	0.0155	(2)
β CMa	12.03	4.370	4.306	3.644	0.167	0.0598	13.5	4.373	4.488	3.529	0.128	0.0538	0.021	(3)
θ Oph	8.04	4.330	3.668	3.948	0.393	0.1067	8.2	4.348	3.745	3.950	0.38	0.1068 - 0.1075	0.012	(4)
HD 192575	13.03	4.395	4.466	3.619	0.225	0.1880	13.0	4.401	4.445	3.662	0.236	...	0.014	(5)
12 Lac	11.35	4.360	4.227	3.661	0.166	0.156	10.0 - 14.4	4.343 - 4.408	...	3.64 - 3.70	...	0.186 - 0.190	0.010 - 0.015	(6)

Notes. The initial metallicity in our models is not shown as it is fixed to 0.014. 12 Lac is shown separately due to its limited capacity to test our forward modelling. For ν Eri, we included the ten frequencies reported by Jerzykiewicz et al. (2005) and modelled by Suárez et al. (2009), who used an initial hydrogen mass fraction of $X = 0.50$ which is too different from ours to merit comparison. Therefore, we compare our model for ν Eri to Ausseloos et al. (2004)'s model with $X = 0.70$. Similarly, we included 12 Lac's $(n, l) = (0, 2)$ multiplet in our modelling, which Desmet et al. (2009) reported but did not fit. Herein we added a frequency detected in the TESS light curve. The literature results of HD 192575 are from Vanlaer et al. (2025) Set 1, which matches our identifications of the radial orders.

References. (1) Dupret et al. (2004); (2) Ausseloos et al. (2004); (3) Mazumdar et al. (2006); (4) Briquet et al. (2007); (5) Vanlaer et al. (2025); (6) Desmet et al. (2009).

the parameter estimation. Notably, there are small differences in $X_{\rm c}$ because our updated nuclear network and rates lead to a larger stellar radius and thus smaller pulsation frequencies. There is also a minor, yet understandable discrepancy in M of HD 129929, β CMa, and ν Eri. This is due to the larger Z in the stellar models of Aerts et al. (2004b), Mazumdar et al. (2006), and Ausseloos et al. (2004). Indeed, Dupret et al. (2004) find a positive relation between Z and M for HD 129929, and Ausseloos et al. (2004) a negative relation for ν Eri, explaining the differences in M we found with our $Z = 0.014$ grid.

For HD 192575, the only validation star without an identified radial mode, we closely match the model of Vanlaer et al. (2025). This confirms that our modelling approach of fixing one frequency first is still effective with a non-radial mode. To verify this further, we re-analysed this star with a different fixed mode and found no differences greater than the uncertainties.

Our procedure consistently leads to the same $n_{\rm pg}$ as those reported in the literature, despite not including the reported $n_{\rm pg}$ in our input. Our identification of KZ Mus's radial mode as $n_{\rm pg} = 1$ also agrees with Handler et al. (2003). For 12 Lac, the three conditions listed above prefer identifying its radial mode with $n_{\rm pg} = 1$, as Dziembowski & Pamyatnykh (2008) did, explaining the 6.70 d^{-1} signal as part of an $l = 2$ multiplet. However, multicolour photometry by Handler et al. (2006) indicates this mode belongs to a $l = 1$ multiplet. With this additional constraint, we unambiguously assigned the radial mode to $n_{\rm pg} = 2$, as also concluded by Desmet et al. (2009). While the agreements confirm the overall reliability of our approach to selecting the radial orders, the case of 12 Lac highlights that radial order identifications of β Cep pulsators are not obvious for some stars. Moreover, it demonstrates the need to manually appraise the modelling results to select the radial orders.

4.4. Summary of modelling results

Satisfied with the performance of our modelling procedure, we applied it to all 38 targets from the sample of Fritzewski et al. (2025). We found a satisfactory asteroseismic model for 31 of these targets, which combined with the five literature stars produces a total sample of 36 β Cep pulsators. However, seven stars could not be properly modelled and were thus removed from our sample. Our inability to find a good model for these seven stars could indicate their mode identifications were incorrect since the identified degrees from Fritzewski et al. (2025) are not absolute. Moreover, rotational splitting can be misidentified by the chance alignment of different modes. Alternatively, these stars may be affected by some process not accounted for in our modelling, such as binary interactions or magnetic fields (Mathis & Bugnet 2023; Das et al. 2024; Guo et al. 2024).

The modelling results of the 36 remaining β Cep pulsators are summarised in Table D.2. A corner plot of the five free parameters is given in Fig. A.1. Our sample covers the parameter space quite well, except in M as only two stars have $M > 20\,M_\odot$. The maximum value of $X_{\rm c}$ is 0.43 so our sample only probes the second half of the main sequence, in line with the shape of the β Cep instability strip (Pamyatnykh 1999; Burssens et al. 2020). A similar range in $X_{\rm c}$ was reported by Fritzewski et al. (2025), who modelled the $T_{\rm eff}$, L and one zonal frequency in 119 β Cep stars based on the identified l of the dominant mode. We compare the modelling outcomes of the stars in both modelled samples in Appendix B.1. While there is an overall agreement in M, our modelling greatly improved the estimates of $X_{\rm c}$.

5. Importance of second-order rotational effects

Thanks to the size of our sample, we can now examine the systematic impact of second-order rotational effects in β Cep forward modelling. Past measurements of $f_{\rm rot}$ from rotational splitting $\Delta f = f_m - f_0$ in β Cep stars relied on first-order Ledoux splitting $\Delta f = m(1 - C_{nl})f_{\rm rot}$, with the Ledoux constant C_{nl} (Ledoux 1951) computed for the best forward model selected using identified zonal frequencies (e.g. Aerts et al. 2003; Dupret et al. 2004; Pamyatnykh et al. 2004; Desmet et al. 2009; Burssens et al. 2023). Even studies that included second-order rotation effects (e.g. Briquet et al. 2007; Dziembowski & Pamyatnykh 2008; Suárez et al. 2009; Vanlaer et al. 2025) estimated $f_{\rm rot}$ a posteriori. In contrast, the rotationally induced asymmetric splitting and zonal frequency shifts play a key role in our forward modelling, notably in the consistent optimisation of $f_{\rm rot}$.

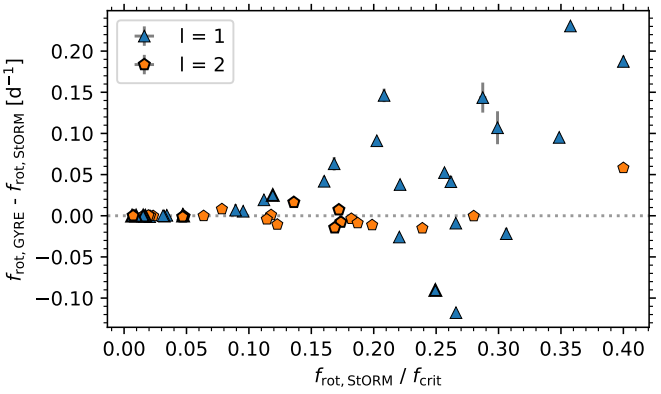

Fig. 4: Difference in rotation frequency from each identified multiplet between our self-consistent modelling using StORM and the a posteriori step with GYRE against the relative rotation rate. Multiplets belonging to a validation stars are outlined in black. The grey dotted line shows where the two estimates agree.

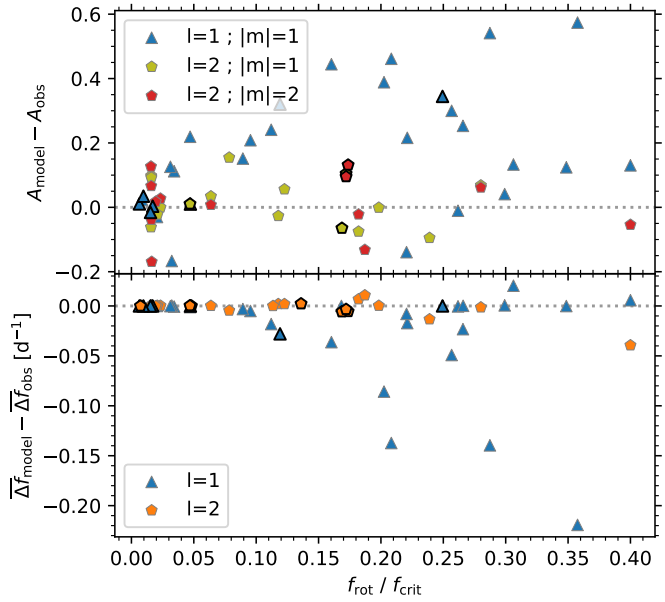

Fig. 5: Difference in asymmetry (top) and mean rotational splitting (bottom) from each rotationally split multiplet between the best model and observations against the relative rotation rate. Multiplets belonging to a validation star are outlined in black. The grey dotted line highlights where the model reproduces the observation.

To evaluate how StORM's inclusion of second-order rotation effects affects the measured $f_{\rm rot}$, we computed C_{nl} in the grid model closest to the statistical model using the oscillation code GYRE version 7.2.1 (Townsend & Teitler 2013). Emulating previous studies, we estimated $f_{\rm rot}$ for each rotationally split multiplet as $f_{\rm rot} = \overline{\Delta f}/(1 - C_{nl})$, with $\overline{\Delta f} = \overline{(f_m - f_0)/m}$ the observed mean rotational splitting. Figure 4 compares these estimates to our consistently optimised $f_{\rm rot}$ from StORM. The two estimates deviate strongly when $f_{\rm rot} > 10\% f_{\rm crit}$. Therefore, second-order effects of rotation on oscillation predictions should not be ignored in β Cep stars rotating faster than approximately $10\% f_{\rm crit}$.

Figure 4 also shows that the optimal $f_{\rm rot}$ found with StORM tends to be smaller than that found with GYRE, especially from $l = 1$ multiplets at higher $f_{\rm rot}$. This is because StORM often predicts highly asymmetric splitting, meaning the splitting of retrograde modes ($m < 0$) is larger than that of prograde modes ($m > 0$). Indeed, StORM's predicted asymmetry tends to be larger than observed for $l = 1$ modes, as shown in the top panel of Fig. 5, though this is partly because we sought multiplets with a small asymmetry in Sect. 2. Consequently, our forward modelling method reproduces the splitting of the retrograde modes reasonably well, yet sometimes underpredicts the prograde mode splitting. Figure 5's bottom panel shows that $\overline{\Delta f}$ is sometimes underestimated. This may imply that we somewhat underestimate $f_{\rm rot}$ for some stars with identified prograde $l = 1$ modes rotating faster than $10\% f_{\rm crit}$.

The observed asymmetries being smaller than predicted may indicate our models lack some crucial physics, for which there are a number of candidates. Firstly, these β Cep stars could possess strong magnetic fields, which counteract the rotationally induced asymmetric splitting (Mathis & Bugnet 2023; Das et al. 2024; Guo et al. 2024). Secondly, StORM's treatment of the 2D processes of rotation and deformation with a 1D second-order perturbative approach may be stretched beyond its limit (Reese et al. 2006; Mombarg et al. 2025). Finally, differential rotation might also affect the asymmetry (Suárez et al. 2006, 2009), while we assumed rigid rotation in our oscillation computations as the rotation profile is unknown a priori.

To examine how including second-order rotation effects and consistently modelling the rotational splitting affects the estimation of stellar parameters besides $f_{\rm rot}$, we repeated our forward modelling with two different methods. Firstly, we re-analysed all stars with $f_{\rm rot}$ consistently optimised for the first-order rotation treatment of GYRE during the forward modelling. Secondly, we tested removing the rotational splitting from the χ^2 cost function. The methods and results from these tests are detailed in Appendix B.2, which are summarised here. The observed zonal frequencies are better reproduced when including the decrease of mode frequencies by the second-order effect of stellar deformation. In this respect, the incorporation of second-order effects clearly improves the forward modelling quality. Moreover, while the inclusion of rotational splitting in the χ^2 cost function worsens the match with the observed zonal frequencies when $f_{\rm rot} > 20\% f_{\rm crit}$, it improves the reproduction of the observed asymmetry and mean splitting at all $f_{\rm rot}$. Therefore, the choice of whether or not to add rotational splitting in the cost function depends on what stellar parameters one prioritises. As this study is primarily concerned with the rotational properties of β Cep stars, we elected to include the rotational splitting in the cost function. Nonetheless, the inability to reproduce all observables at high $f_{\rm rot}$ introduces an additional source of systematic uncertainty. Finally, the differences in all stellar parameters, except $f_{\rm rot}$, produced by these different modelling approaches are generally small, indicating that these additional systematic uncertainties are modest and justifying the exploitation of the results presented below.

6. Behaviour of core mass and rotation rate

We now look for trends in the stellar structure parameters of β Cep stars. In particular, we look into the mass of the convective core given its importance to the star's later evolution and its chemical yields (Hirschi et al. 2005; Pedersen 2022; Brinkman et al. 2025). We also focus on the internal rotation to facilitate future angular momentum transport studies for a sample of high-mass stars.

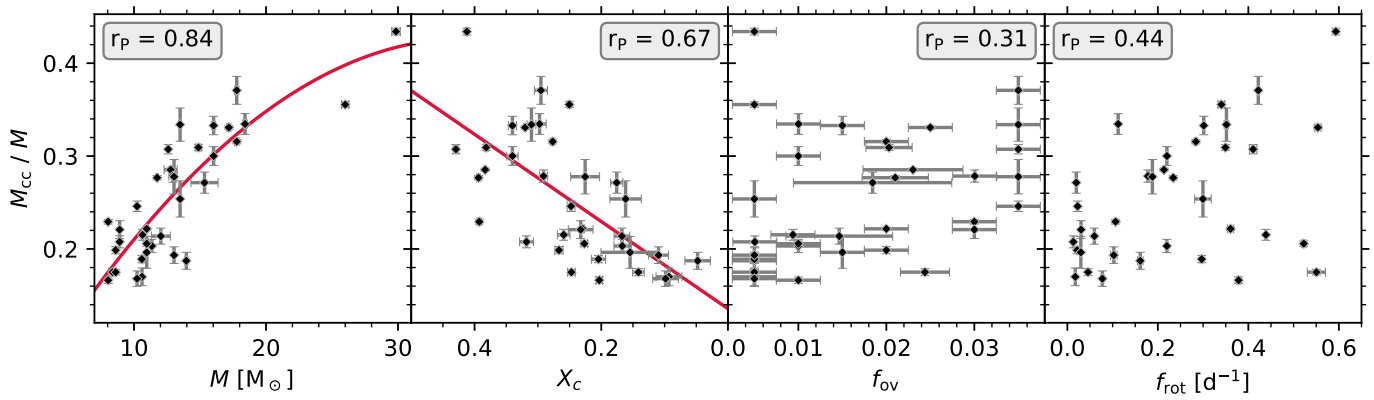

Fig. 6: Convective core mass relative to total stellar mass against the total mass, central hydrogen mass fraction, overshoot parameter, and rotation frequency. Red lines show a quadratic and linear fit against total mass and central hydrogen mass fraction, respectively. Boxes display the Pearson correlation coefficients between relative convective core mass and each considered parameter.

6.1. Convective core mass

The convective cores of massive stars shrink as they evolve along the main sequence due to the changing opacity as hydrogen is fused into helium by the CNO cycle. This has been studied from asteroseismology of γ Dor (Mombarg et al. 2021) and SPB stars (Pedersen 2022). With the forward modelling results of our β Cep sample, we can now asteroseismically calibrate the behaviour of the convective core mass $M_{\rm cc}$ across a higher mass range. To that end, we fitted the inferred asteroseismic $M_{\rm cc}$ relative to the total stellar mass M quadratically against M and linearly against $X_{\rm c}$. These relations, shown in Fig. 6, are given by

$$M_{\rm cc}/M = -3.4(1.8)\,10^{-4}\left(\frac{M}{\rm M_\odot}\right)^2 + 0.0241(63)\,\frac{M}{\rm M_\odot} + 0.039(50)$$

$$M_{\rm cc}/M = 0.469(87)\,X_{\rm c} + 0.136(24)$$

$$M_{\rm cc}/M = -3.90(91)\,10^{-4}\left(\frac{M}{\rm M_\odot}\right)^2 + 0.0236(32)\,\frac{M}{\rm M_\odot} + 0.328(34)\,X_{\rm c} - 0.064(26)$$

The coefficients of determination of these three relations are 0.73, 0.45 and 0.93 respectively, indicating that the bivariate fit explains most of the variability in $M_{\rm cc}$. The value of $M_{\rm cc}$ increases with $f_{\rm ov}$ as overshooting provides the core access to more hydrogen drawn in from the envelope. Our results are in agreement with Johnston (2021), who compared the seismic $M_{\rm cc}$ with those of eclipsing binaries to conclude that a variety of core masses occurs across a wide range of stars with convective cores.

Finally, a significant correlation between $M_{\rm cc}$ and $f_{\rm rot}$ occurs, following the positive $f_{\rm rot} - X_{\rm c}$ correlation seen in Fig. A.1. This relation between $f_{\rm rot}$ and $X_{\rm c}$ reflects the decrease of the internal rotation rate along the main sequence, in line with the large sample of intermediate-mass main sequence stars in Aerts (2021); Aerts et al. (2025). Another significant correlation included in Fig. A.1 is due to $f_{\rm ov}$ decreasing as $X_{\rm c}$ decreases, indicating that core overshooting weakens as the star evolves. Both phenomena are likely connected because parametrised core overshooting is merely a reflection of core boundary mixing due to a multitude of instabilities occurring in this transition layer, many of which are caused by the local rotation rate (see Heger et al. 2000; Aerts et al. 2019, for extensive discussions of these instabilities).

6.2. Specific angular momentum of β Cep stars

The evolution of the specific angular momentum $J/M = 4\pi/3\, f_{\rm rot} R^2$ of a population of stars is used to study initial stellar rotation rates and angular momentum losses. Kraft (1967) discussed a decrease of $f_{\rm rot}$ with age in solar-type stars, indicating efficient angular momentum loss due to magnetic winds. The relation between J/M and stellar mass M, in particular the 'Kraft break' around 1.3 $\rm M_\odot$, has also been used to examine how the efficiency of angular momentum loss depends on stellar structure (Kawaler 1987, 1988). Recently Aerts (2025) studied asteroseismically deduced J/M values for approximately 3000 pulsating main sequence stars with masses between 1.3 and 9 $\rm M_\odot$. From the near-core rotation rate and assuming quasi-rigid rotation, they found a another break in the $J/M(M)$ relation by the end of the main sequence around $2.5 \pm 0.2\,\rm M_\odot$. This second break is interpreted as due to the disappearance of the convective envelope for stars with $M \gtrsim 2.5\,\rm M_\odot$.

Using our sample of β Cep stars with masses between 8 and 30 $\rm M_\odot$, we test the upper limit of J/M in a higher mass regime. Figure 7 displays the $J/M(M)$ and $J/M(X_{\rm c})$ relations along with the high-mass upper limit in $J/M(M)$ presented by Aerts (2025). The massive β Cep stars obey this upper limit, in agreement with the interpretation by Aerts (2025). For β Cep pulsators, the assumption of quasi-rigid rotation may not be appropriate though, introducing a major uncertainty on the presented J/M. Nonetheless, as the $J/M(M)$ upper limit remains over 50% above the $J/M(M)$ of our stars, comparable to the typical level of differential rotation in β Cep stars (Burssens et al. 2023, cf. Sect. 7), the total J/M likely still lies below the upper limit.

The right panel of Fig. 7 shows that there is no sign of J/M increasing as $X_{\rm c}$ decreases. In contrast, Aerts (2025) finds that J/M increases as $X_{\rm c}$ decreases for the more massive stars in their sample of intermediate-mass stars. That increase either means that some of these stars gained angular momentum from binary interactions or developed differential rotation with the interior rotating more rapidly than the surface. The lack of such a relation in our sample may be due to the small sample size or may indicate that the internal rotation profiles of our high-mass β Cep stars are different from those of the intermediate-mass stars of Aerts (2025). We investigate this in the next Section.

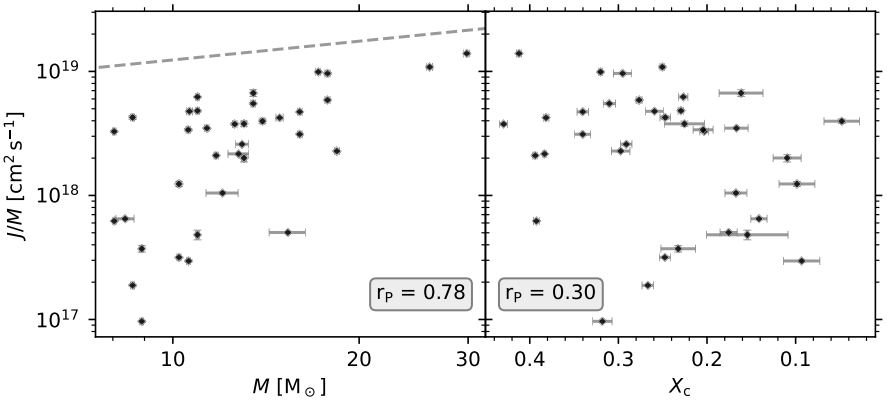

Fig. 7. Specific angular momentum of each star, assuming rigid rotation at the rate measured from the forward modelling, against its mass (left) and core hydrogen mass fraction (right). On the left panel, we include the upper limit on the specific angular momentum for stars more massive than 2.5 $M_\odot$ derived by Aerts (2025) as a grey dashed line. Boxes show the Pearson correlation coefficients.

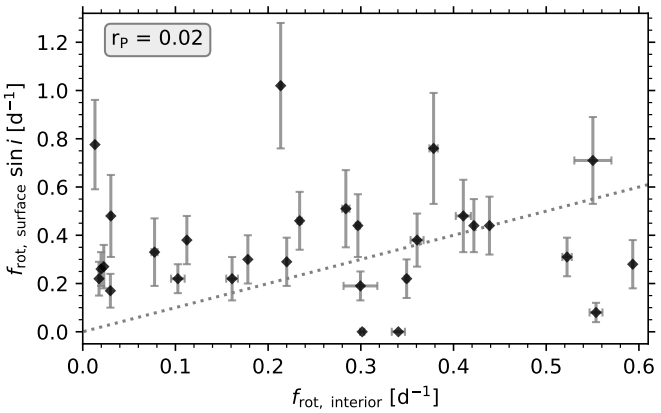

Fig. 8: Projected surface rotation frequency against the interior rotation frequency when modelling all identified multiplets. The grey dotted line marks where the two measurements are equal. The Pearson correlation coefficient is included in a box. Two stars were assigned a surface rotation velocity of zero by the ESP-HS pipeline, indicating that rotational broadening was not detected.

7. Differential rotation constraints in 17 β Cep stars

We now seek to constrain the rotation profiles in a subsample of our β Cep stars. From our optimised internal rotation frequencies $f_{\mathrm{rot,interior}}$ and spectroscopic measurements of the projected surface velocities $f_{\mathrm{rot,surface}} \sin i$, we place an upper bound on the envelope-to-surface rotation ratio. Figure 8 shows the relation between these two rotation measurements for 29 stars with an available estimate of $f_{\mathrm{rot,surface}} \sin i$. Notably, they are uncorrelated, in part because $f_{\mathrm{rot,surface}} \sin i$ is only a lower limit of $f_{\mathrm{rot,surface}}$. Counteracting this, the surface velocity is measured from the width of spectroscopic lines, which are also broadened by pulsations, so $f_{\mathrm{rot,surface}}$ of our high-amplitude β Cep stars is potentially overestimated instead. These systematic errors and the large uncertainties cloud any relation between internal and surface rotation frequency. Therefore, we turn to purely asteroseismic constraints on the internal rotation profile, which are unaffected by unknown projection factors.

As the rotation profile of β Cep stars is not known a priori, we assumed a constant rotation profile in our oscillation calculations. In order to constrain the internal differential rotation of stars despite using rigidly rotating models, we re-analysed of the 17 stars with more than one non-radial mode once per rotationally split multiplet. Each time, we fitted all identified zonal mode frequencies, but only one multiplet's rotational splitting Δf. Consequently, f_{rot} is optimised for only that multiplet when finding the optimal model for each evolutionary track. For consistency, the statistical parameter estimation of f_{rot} still used the $\exp(-\chi^2/2)$ weights found when modelling all multiplets' Δf, though X_c can vary slightly to account for different rotationally induced frequency shifts. Next, we computed the multiplet's rotational sensitivity kernel K_{nl} from the `MESA` output closest to the statistical model produced by modelling all multiplets. Figure C.1 shows some examples of sensitivity kernels from different non-radial modes. The left panel of Fig. 9 shows f_{rot} for each multiplet against the radius r where it is most sensitive. The right panel plots the rotation ratio with the mode that is most sensitive closest to the surface.

Strong radial differential rotation is common in our sample of β Cep pulsators, as f_{rot} measurements vary by more than 10% in 14 of 17 stars. Even the three stars with a small difference in f_{rot}, such as θ Oph (shown in red in Fig. 9), might still be differential rotators. As Fig. C.1 shows its two multiplets probe the same layers of the envelope, it could still feature differential rotation in unprobed regions. While the outward rotation gradient $\frac{\partial f_{\mathrm{rot}}}{\partial r}$ is more commonly negative, as observed before (Burssens et al. 2023), there are nevertheless four stars for which f_{rot} grows with r by over 10%. Such a strong outward increase in f_{rot} has not been detected in β Cep pulsators before. Only in the aforementioned θ Oph has a positive rotation gradient been suggested before, albeit by only 5% (Briquet et al. 2007).

That we so commonly detect significant differential rotation in our sample is somewhat surprising as there are three notable biases against it. Firstly, the low-order modes in β Cep stars are usually sensitive to broad regions of the stellar envelope, as shown in Fig. C.1. When the sensitivity kernels of two multiplets overlap, the difference in their optimal f_{rot} is diminished as they both average f_{rot} over the same layers. Secondly, there is a selection bias in our mode identification from rotational splitting. β Cep stars with candidate multiplets with rotational splitting different by more than a factor two were not included in our sample. Finally, our modelling is set up to reproduce all observed rotational splitting based on models assuming homogeneous rotation. Consequently, the difference in f_{rot} required to optimally reproduce the splitting of each multiplet individual is reduced. That we detect rotation differences greater than 10% in 14 out of 17 stars despite these biases strengthens the conclusion that strong radial differential rotation is common in evolved β Cep stars.

Remarkably, four of the six stars with two multiplets probing $r/R_* > 0.5$ display an outwardly increasing rotation fre-

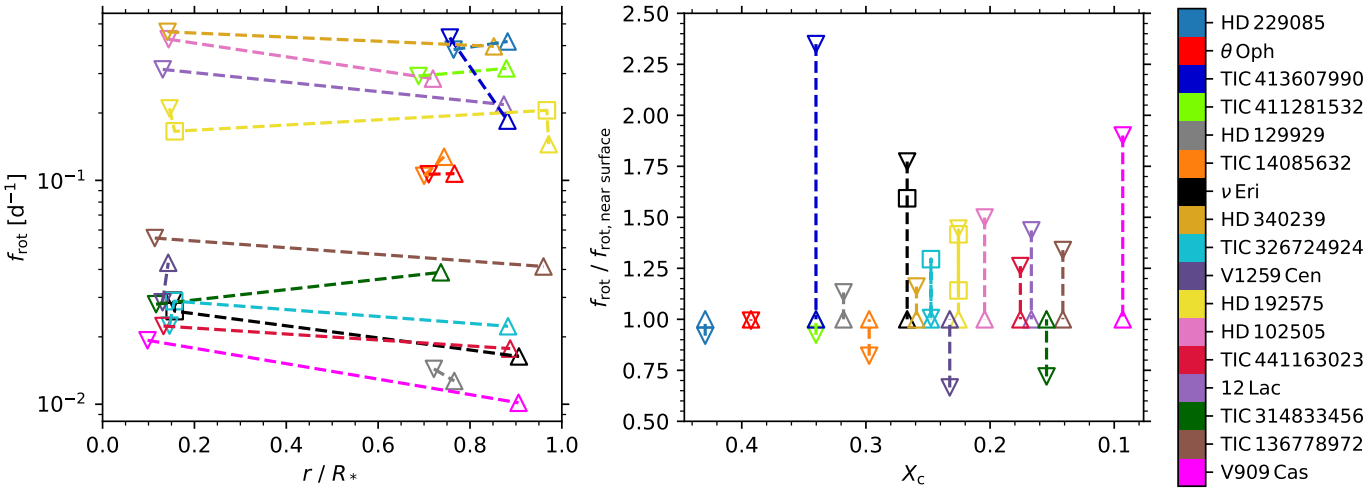

Fig. 9: Interior differential rotation in 17 stars with several rotationally split multiplets. The left panel shows the rotation frequency from a rotationally split mutliplet at the radius where that multiplet is most sensitive. The mode most sensitive nearest the core is represented by a downward pointing triangle, the mode most sensitive nearest the surface by an upward triangle, and any other mode by a square. The right panel shows these rotation rates are normalised by the rotation rate nearest the surface against the core hydrogen mass fraction. Each star has a unique colour indicated in the colourbar, which is sorted by central hydrogen mass fraction.

quency, with the notable exceptions of TIC 413607990 (lime) and HD 129929 (grey). These four stars could have undergone accretion during binary interactions. Meanwhile, most stars with a multiplet probing near the core and another the upper envelope have a negative rotation gradient, except for TIC 314833456 (dark green). Combined, these trends may indicate that the typical rotation profile of β Cep pulsators is non-monotonic, featuring a relatively rapidly rotating core and a slower envelope with $\frac{\partial f_{\rm rot}}{\partial r} > 0$. The two of the three stars with more than two rotationally split multiplets, HD 192575 (yellow) and ν Eri (black), also produce both positive and negative $\frac{\partial f_{\rm rot}}{\partial r}$. Indeed, the rotation inversions of HD 192575 by Vanlaer et al. (2025) show that it has a core-to-envelope rotation ratio no greater than two and its rotation profile is not monotonic. Furthermore, the 2D hydrodynamical simulations of convection and internal gravity waves in a 7 $M_\odot$ model of Rogers & Ratnasingam (2025) produce a similar rotation profile. In short, there is mounting evidence that non-monotonic differential rotation is common in β Cep stars, though not ubiquitous.

Further testing the non-monotonicity of β Cep rotation profiles would benefit from measurements of differential rotation in yet more β Cep stars, particularly with an eye on identifying and observationally calibrating the underlying angular momentum transport mechanisms. Therefore, the rotation gradient should be observed at different stages along the main sequence. However, this is limited by β Cep stars only occurring in the second half of the main sequence (cf. Sect. 4.4). On top of that, the mode excitation of β Cep pulsations is also not uniform throughout their evolution. As seen in the right panel of Fig. 9, the six stars that probe at different points in the upper envelope are the six least evolved stars of this subsample of 17 with $0.28 < X_c < 0.43$. Meanwhile, the ten stars that probe both the near-core region and outer envelope are all more evolved with $X_c < 0.28$. Indeed, the computations of mode excitation by Rehm et al. (2024) in a 9 $M_\odot$ stellar model indicate that several p-modes, which probe the envelope, are only excited while the star is young. Once it is more evolved, more and higher-order g-modes, which are most sensitive to the near-core layers, become excited. Consequently, observing the envelope rotation gradient in evolved and the core-to-envelope rotation ratio in relatively young β Cep pulsators may be difficult. Nonetheless, their value to constraining angular momentum transport makes seeking such detections a worthwhile effort regardless.

In conclusion, measurable differential rotation is common in β Cep stars. The level of differentiality we could measure in our sample is below a factor 2.5. This implies that the uncertainty on J/M in Fig. 7 due to the radial differential rotation is small enough that our stars should still obey the upper limit of Aerts (2025). Moreover, as differential rotation in β Cep stars appears to be non-monotonic and β Cep pulsations probe a variety of different layers, the presented J/M may be overestimated. Therefore, the conclusions from Sect. 6.2 regarding the specific angular momentum remain valid.

8. Summary and conclusions

To maximally exploit the massive β Cep pulsators' potential to observationally constrain angular momentum transport on the main sequence, we present a sample of 36 asteroseismically modelled β Cep stars. This marks the first time a population of β Cep stars has been forward modelled in such detail. For most stars in this sample, Fritzewski et al. (2025) provided partial mode identifications which we complemented with identifications from rotational splitting. For our forward modelling, we created a new grid of `MESA` main sequence models with a wide range in mass, age, core overshoot, and envelope mixing. The oscillations in these models were computed using the state-of-the-art `StORM` code, which includes second-order rotation effects. Using these improved oscillation predictions, we developed the first forward modelling approach for β Cep pulsators that consistently takes rotation into account.

Making use of the size of our sample, we asteroseismically calibrated the convective core mass's evolution and mass-dependency. Herein, we found that the core overshoot weakens with age, reflecting the shrinking core of these massive main sequence stars. Consequently, stellar models should ideally implement some time-dependent core overshooting scheme. Like

in intermediate-mass main sequence stars, the rotation rate decreases as the stars evolve. Moreover, our β Cep stars obey the specific angular momentum relations of intermediate-mass stars.

One notable shortcoming of our modelling is our overestimation of the asymmetry of rotationally split dipole multiplets, indicating some important physics is missing in our modelling. Internal magnetic fields are an obvious candidate as they are known to reduce the asymmetry of rotationally split multiplets. However, unambiguously disentangling the effects of both magnetism and rotation from asymmetries alone is difficult. This issue is alleviated if a multiplet displays both rotational and magnetic splitting, resulting in more than $2l + 1$ components. HD 192575 is currently the only known β Cep star with such splitting (Vandersnickt et al. submitted). Consequently, a population level study including magnetic effects is not plausible until more β Cep pulsators with magnetic splitting are discovered.

An observational avenue to continue improving our understanding of β Cep stars is to further expand the sample to fill out the broad parameter space. In particular, there is still a shortage of β Cep stars more massive than $20\,M_\odot$. Further, more targets with enough rotationally split multiplets to measure the internal rotation rate near the core and throughout the envelope at different ages would also be highly beneficial. The upcoming PLATO space telescope (Rauer et al. 2025) is expected to provide the necessary photometry to detect the pulsation frequencies of several dozen β Cep pulsators with high precision (Nascimbeni et al. 2025). Meanwhile, both ground- and space-based multi-colour observations of β Cep stars have proven their capability to identify those pulsation signals. As shown by our work, these mode identifications can then be further refined from rotational splitting.

We successfully constrained radial differential rotation in 17 stars, increasing the sample of β Cep stars with purely asteroseismic measurements of differential rotation more than threefold. An overall trend emerged suggesting that the inner region near the convective core rotates faster than the envelope. For the few stars offering the information, we find that the rotation rate often 5increases outwardly in the envelope, as expected for stars having experienced accretion in their recent past and/or being subject to the action of internal gravity waves. Combined with rotation inversions and rotation profiles in multi-dimensional hydrodynamical simulations, we conclude that non-monotonic differential rotation is common in β Cep stars. Testing which angular momentum transport mechanisms can explain these rotation profiles will require more thorough stellar modelling using new generations of stellar structure and evolution models with realistic transport mechanisms in order to verify if they reproduce all the observed rotational splitting.

Acknowledgements. MV thanks Hannah Brinkman for her advice in adapting our `MESA` inlists and for designing the nuclear network and acknowledges Ehsan Moravveji for his assistance in setting up the `MESA` grid computations. He also thanks Noi Shitrit, Tami Rogers, Miriam Rodriguez-Sanchez, Jelle Vandersnickt, Zhao Guo, and Pablo Huijse for useful conversations and Joey Mombarg and Michel Rieutord for helpful comments. The `MESA` and `StORM` computations were done at the Flemish Supercomputer Centre (VSC). MV has received funding from the KU Leuven Research Council (doctoral mandate grant DB/24/008). VV gratefully acknowledges support from the Research Foundation Flanders (FWO) under grant agreement N°1156923N (PhD Fellowship). DJF and CA acknowledge support from the Flemish Government under the long-term structural Methusalem funding program by means of the project SOUL: Stellar evolution in full glory, grant METH/24/012 at KU Leuven. MV and CA acknowledge financial support from the European Research Council (ERC) under the Horizon Europe programme (Synergy Grant agreement N°101071505: 4D-STAR). While partially funded by the European Union, views and opinions expressed are however those of the authors only and do not necessarily reflect those of the European Union or the European Research Council. Neither the European Union nor the granting authority can be held responsible for them. CA also acknowledges the Belgian Federal Science Policy Office (BELSPO) for the provision of financial support in the framework of the PRODEX Programme of the European Space Agency (ESA).

Software: This research made use of the `astropy` (Astropy Collaboration et al. 2022), `h5py` (Collette 2013), `matplotlib` (Hunter 2007), `NumPy` (Harris et al. 2020), `pandas` (Wes McKinney 2010), and `SciPy` (Virtanen et al. 2020) `Python` packages. We used the `MESA` (Paxton et al. 2011, 2013, 2015, 2018, 2019; Jermyn et al. 2023) stellar structure and evolution code to compute our new grid of stellar models and the codes `StORM` (Vanlaer et al. submitted) and `GYRE` (Townsend & Teitler 2013) to perform the oscillation computations.

References

Aerts, C. 2021, Reviews of Modern Physics, 93, 015001
Aerts, C. 2025, arXiv e-prints, arXiv:2511.02909
Aerts, C., Christensen-Dalsgaard, J., & Kurtz, D. W. 2010, Asteroseismology (Springer Netherlands)
Aerts, C. & De Cat, P. 2003, Space Sci. Rev., 105, 453
Aerts, C., De Cat, P., Handler, G., et al. 2004a, MNRAS, 347, 463
Aerts, C., Marchenko, S. V., Matthews, J. M., et al. 2006, ApJ, 642, 470
Aerts, C., Mathis, S., & Rogers, T. M. 2019, ARA&A, 57, 35
Aerts, C., Molenberghs, G., Michielsen, M., et al. 2018, ApJS, 237, 15
Aerts, C., Thoul, A., Daszyńska, J., et al. 2003, Science, 300, 1926
Aerts, C. & Tkachenko, A. 2024, A&A, 692, R1
Aerts, C., Van Reeth, T., Mombarg, J. S. G., & Hey, D. 2025, A&A, 695, A214
Aerts, C., Waelkens, C., Daszyńska-Daszkiewicz, J., et al. 2004b, A&A, 415, 241
Asplund, M., Grevesse, N., Sauval, A. J., & Scott, P. 2009, ARA&A, 47, 481
Astropy Collaboration, Price-Whelan, A. M., Lim, P. L., et al. 2022, ApJ, 935, 167
Augustson, K. C. & Mathis, S. 2019, ApJ, 874, 83
Ausseloos, M., Scuflaire, R., Thoul, A., & Aerts, C. 2004, MNRAS, 355, 352
Auvergne, M., Bodin, P., Boisnard, L., et al. 2009, A&A, 506, 411
Bessila, L., Deckx van Ruys, A., Buriasco, V., et al. 2025, A&A, 700, A25
Borucki, W. J., Koch, D., Basri, G., et al. 2010, Science, 327, 977
Brinkman, H. E., Tkachenko, A., & Aerts, C. 2025, A&A, 702, A119
Briquet, M., Lefever, K., Uytterhoeven, K., & Aerts, C. 2005, MNRAS, 362, 619
Briquet, M., Morel, T., Thoul, A., et al. 2007, MNRAS, 381, 1482
Briquet, M., Neiner, C., Aerts, C., et al. 2012, MNRAS, 427, 483
Briquet, M., Uytterhoeven, K., Morel, T., et al. 2009, A&A, 506, 269
Burssens, S., Bowman, D. M., Michielsen, M., et al. 2023, Nature Astronomy, 7, 913
Burssens, S., Simón-Díaz, S., Bowman, D. M., et al. 2020, A&A, 639, A81
Chandrasekhar, S. 1933, MNRAS, 93, 390
Collette, A. 2013, Python and HDF5 (O'Reilly Media)
Cotton, D. V., Buzasi, D. L., Aerts, C., et al. 2022, Nature Astronomy, 6, 154
Cyburt, R. H., Amthor, A. M., Ferguson, R., et al. 2010, ApJS, 189, 240
Das, S. B., Einramhof, L., & Bugnet, L. 2024, A&A, 690, A217
De Ridder, J., Telting, J. H., Balona, L. A., et al. 2004, MNRAS, 351, 324
Degroote, P., Briquet, M., Catala, C., et al. 2009, A&A, 506, 111
Deheuvels, S., Doğan, G., Goupil, M. J., et al. 2014, A&A, 564, A27
Desmet, M., Briquet, M., Mazumdar, A., & Aerts, C. 2006, Communications in Asteroseismology, 147, 113
Desmet, M., Briquet, M., Thoul, A., et al. 2009, MNRAS, 396, 1460
Di Mauro, M. P., Ventura, R., Cardini, D., et al. 2016, ApJ, 817, 65
Dupret, M. A., Thoul, A., Scuflaire, R., et al. 2004, A&A, 415, 251
Dziembowski, W. A. & Pamyatnykh, A. A. 2008, MNRAS, 385, 2061
Eckart, C. 1961, Physics of Fluids, 4, 791
Eze, C. I. & Handler, G. 2024, ApJS, 272, 25
Ferguson, J. W., Alexander, D. R., Allard, F., et al. 2005, ApJ, 623, 585
Fouesneau, M., Frémat, Y., Andrae, R., et al. 2023, A&A, 674, A28
Fritzewski, D. J., Vanrespaille, M., Aerts, C., et al. 2025, A&A, 698, A253
Gaia Collaboration, Prusti, T., de Bruijne, J. H. J., et al. 2016, A&A, 595, A1
Gaia Collaboration, Vallenari, A., Brown, A. G. A., et al. 2023, A&A, 674, A1
García, R. A. & Ballot, J. 2019, Living Reviews in Solar Physics, 16, 4
Guo, Z., Bedding, T. R., Pamyatnykh, A. A., et al. 2024, MNRAS, 535, 2927
Handler, G., Jerzykiewicz, M., Rodríguez, E., et al. 2006, MNRAS, 365, 327
Handler, G., Shobbrook, R. R., Jerzykiewicz, M., et al. 2004, MNRAS, 347, 454
Handler, G., Shobbrook, R. R., & Mokgwetsi, T. 2005, MNRAS, 362, 612
Handler, G., Shobbrook, R. R., Uytterhoeven, K., et al. 2012, MNRAS, 424, 2380
Handler, G., Shobbrook, R. R., Vuthela, F. F., et al. 2003, MNRAS, 341, 1005
Harris, C. R., Millman, K. J., van der Walt, S. J., et al. 2020, Nature, 585, 357
Heger, A., Langer, N., & Woosley, S. E. 2000, ApJ, 528, 368
Hekker, S. & Christensen-Dalsgaard, J. 2017, A&A Rev., 25, 1
Hey, D. & Aerts, C. 2024, A&A, 688, A93
Heynderickx, D., Waelkens, C., & Smeyers, P. 1994, A&AS, 105, 447
Hirschi, R., Meynet, G., & Maeder, A. 2005, A&A, 443, 581

Hunter, J. D. 2007, Computing in Science & Engineering, 9, 90
Irwin, A. W. 2004, The FreeEOS Code for Calculating the Equation of State for Stellar Interiors I: An Improved EFF-Style Approximation for the Fermi-Dirac Integrals, https://freeeos.sourceforge.net/
Jermyn, A. S., Bauer, E. B., Schwab, J., et al. 2023, ApJS, 265, 15
Jermyn, A. S., Schwab, J., Bauer, E., Timmes, F. X., & Potekhin, A. Y. 2021, ApJ, 913, 72
Jerzykiewicz, M., Handler, G., Shobbrook, R. R., et al. 2005, MNRAS, 360, 619
Johnston, C. 2021, A&A, 655, A29
Kawaler, S. D. 1987, PASP, 99, 1322
Kawaler, S. D. 1988, ApJ, 333, 236
Kraft, R. P. 1967, ApJ, 150, 551
Kurtz, D. W. 2022, ARA&A, 60, 31
Kurtz, D. W., Saio, H., Takata, M., et al. 2014, MNRAS, 444, 102
Labadie-Bartz, J., Handler, G., Pepper, J., et al. 2020, AJ, 160, 32
Ledoux, P. 1951, ApJ, 114, 373
Lee, U. & Baraffe, I. 1995, A&A, 301, 419
Li, G., Aerts, C., Bedding, T. R., et al. 2024, A&A, 686, A142
Li, G., Van Reeth, T., Bedding, T. R., et al. 2020, MNRAS, 491, 3586
Maeder, A. 2009, Physics, Formation and Evolution of Rotating Stars
Mathis, S. & Bugnet, L. 2023, A&A, 676, L9
Mathis, S. & Zahn, J. P. 2004, A&A, 425, 229
Mathis, S. & Zahn, J. P. 2005, A&A, 440, 653
Mazumdar, A., Briquet, M., Desmet, M., & Aerts, C. 2006, A&A, 459, 589
Mombarg, J. S. G., Van Reeth, T., & Aerts, C. 2021, A&A, 650, A58
Mombarg, J. S. G., Vanlaer, V., Das, S. B., et al. 2025, arXiv e-prints, arXiv:2511.09617
Moravveji, E., Aerts, C., Pápics, P. I., Triana, S. A., & Vandoren, B. 2015, A&A, 580, A27
Nascimbeni, V., Piotto, G., Cabrera, J., et al. 2025, A&A, 694, A313
Osaki, Y. 1975, PASJ, 27, 237
Pamyatnykh, A. A. 1999, Acta Astron., 49, 119
Pamyatnykh, A. A., Handler, G., & Dziembowski, W. A. 2004, MNRAS, 350, 1022
Paxton, B., Bildsten, L., Dotter, A., et al. 2011, ApJS, 192, 3
Paxton, B., Cantiello, M., Arras, P., et al. 2013, ApJS, 208, 4
Paxton, B., Marchant, P., Schwab, J., et al. 2015, ApJS, 220, 15
Paxton, B., Schwab, J., Bauer, E. B., et al. 2018, ApJS, 234, 34
Paxton, B., Smolec, R., Schwab, J., et al. 2019, ApJS, 243, 10
Pedersen, M. G. 2022, ApJ, 930, 94
Pedersen, M. G., Aerts, C., Pápics, P. I., et al. 2021, Nature Astronomy, 5, 715
Pedersen, M. G., Escorza, A., Pápics, P. I., & Aerts, C. 2020, MNRAS, 495, 2738
Rauer, H., Aerts, C., Cabrera, J., et al. 2025, Experimental Astronomy, 59, 26
Reese, D., Lignières, F., & Rieutord, M. 2006, A&A, 455, 621
Rehm, R., Mombarg, J. S. G., Aerts, C., et al. 2024, A&A, 687, A175
Ricker, G. R., Winn, J. N., Vanderspek, R., et al. 2015, Journal of Astronomical Telescopes, Instruments, and Systems, 1, 014003
Rogers, T. M., Lin, D. N. C., McElwaine, J. N., & Lau, H. H. B. 2013, ApJ, 772, 21
Rogers, T. M. & McElwaine, J. N. 2017, ApJ, 848, L1
Rogers, T. M. & Ratnasingam, R. P. 2025, ApJ, 983, L38
Saio, H. 1981, ApJ, 244, 299
Scuflaire, R. 1974, A&A, 36, 107
Seaton, M. J. 2005, MNRAS, 362, L1
Shi, X.-d., Qian, S.-b., Zhu, L.-y., et al. 2024, ApJS, 271, 28
Shibahashi, H. & Aerts, C. 2000, ApJ, 531, L143
Shitrit, N. & Arcavi, I. 2024, AJ, 167, 65
Shobbrook, R. R., Handler, G., Lorenz, D., & Mogorosi, D. 2006, MNRAS, 369, 171
Suárez, J. C., Goupil, M. J., & Morel, P. 2006, A&A, 449, 673
Suárez, J. C., Moya, A., Amado, P. J., et al. 2009, ApJ, 690, 1401
Takata, M. 2006, PASJ, 58, 893
Talon, S., Zahn, J. P., Maeder, A., & Meynet, G. 1997, A&A, 322, 209
Tassoul, J.-L. 1978, Theory of rotating stars (Princeton University Press)
Tayler, R. J. 1973, MNRAS, 165, 39
Telting, J. H., Aerts, C., & Mathias, P. 1997, A&A, 322, 493
Thoul, A., Aerts, C., Dupret, M. A., et al. 2003, A&A, 406, 287
Townsend, R. H. D. & Teitler, S. A. 2013, MNRAS, 435, 3406
Triana, S. A., Corsaro, E., De Ridder, J., et al. 2017, A&A, 602, A62
Triana, S. A., Moravveji, E., Pápics, P. I., et al. 2015, ApJ, 810, 16
Vandersnickt, J., Vanlaer, V., Vanrespaille, M., & Aerts, C. submitted, A&A
Vanlaer, V., Bowman, D. M., Burssens, S., et al. 2025, A&A, 701, A5
Vanlaer, V., Mombarg, J., Guo, Z., & Townsend, R. submitted, A&A
Virtanen, P., Gommers, R., Oliphant, T. E., et al. 2020, Nature Methods, 17, 261
Wes McKinney. 2010, in Proceedings of the 9th Python in Science Conference, ed. Stéfan van der Walt & Jarrod Millman, 56 – 61

Appendix A: Parameter space

Figure A.1 shows a corner plot of the five free parameters in our modelling. These distributions and some of the correlations were already discussed in Sects. 4.4 and 6.1, respectively. Here we examine some of the remaining correlations or lack thereof.

The Pearson correlation coefficients with the initial mass M reported in Fig. A.1 are dominated by the two most massive stars. If these two targets are neglected, the correlations with $f_{\rm rot}$ and $X_{\rm c}$ become greatly weakened and are no longer significant. However, there is then a significant positive correlation between M and $\log D_{\rm mix,0}$, reflecting how the mixing coefficients must be greater in more massive stars to mix the greater mass over a longer radius. This justifies our decision to increase $\log D_{\rm mix,0}$ for the models with $M > 13.03\,{\rm M}_\odot$ (see Sect. 3.1), although how we constructed the $\log D_{\rm mix,0}$ parameter grid is also partly responsible for the relation with M.

Besides the correlation between $f_{\rm ov}$ and $X_{\rm c}$ discussed in Sect. 6.1, there is no significant correlations including either of the mixing parameters $f_{\rm ov}$ or $\log D_{\rm mix,0}$, which would require a Pearson correlation coefficient $|r_{\rm P}| > 0.33$. Notably, $f_{\rm ov}$ is not significantly negatively correlated with $f_{\rm rot}$, despite theoretical work suggesting that rotation can reduce the efficiency of convection and core-boundary mixing (Tayler 1973; Augustson & Mathis 2019; Bessila et al. 2025).

There are several causes behind this lack of clear relations. Firstly, not all β Cep pulsations are sensitive to the envelope (e.g. the top right panel of Fig. C.1), resulting in $\log D_{\rm mix,0}$ being difficult to constrain in some β Cep stars. Secondly, the diversity inherent in the β Cep pulsation class with its wide range in mass, age, and rotation rate complicates the relations within this broad parameter space. Thirdly, said broad parameter space is not covered uniformly or completely by our sample, which features a broad gap in the mass range between approximately 20 and 25 ${\rm M}_\odot$, visible in the mass histogram of Fig. A.1. Fourthly, due to the limited number of observational constraints on many stars, we did not include the initial metallicity as a fit parameter. β Cep pulsators have a fairly broad range of metallicities which significantly impact the estimates of their masses and ages (e.g., Aerts et al. 2004b; Ausseloos et al. 2004), introducing a source of systematic uncertainty. Finally, differential rotation is common in β Cep stars, which combined with the diverse probing sensitivity of their low-order modes means the rotation rates we measured may not be representative of the star as a whole, potentially weakening relations with $f_{\rm rot}$.

Appendix B: Different modelling approaches

Appendix B.1: Comparison to Fritzewski et al. (2025)

Here we seek to test how the addition of more identified frequencies and our more intricate modelling approach improves upon the modelling of Fritzewski et al. (2025). For the stars in both samples, we compare three essential parameters in Fig. B.1. Overall, there is a clear agreement in the stellar mass M, except at the highest and lowest masses. This is because Fritzewski et al. (2025) used the stellar model grid of Burssens et al. (2023) which only includes M in the range $9\,{\rm M}_\odot \leq M \leq 21.5\,{\rm M}_\odot$, while these stars' masses range from $8\,{\rm M}_\odot$ to $30\,{\rm M}_\odot$. For the central hydrogen mass fraction $X_{\rm c}$ however, the differences are significant, demonstrating that this work significantly improved the estimates of $X_{\rm c}$ and therefore the age. This superior $X_{\rm c}$ constraint also results in an improved estimate for the convective core mass due to the strong relation with $X_{\rm c}$ discussed in Sect. 6.1.

Appendix B.2: Further evaluating the impact of second-order rotation effects

As shown in Sect. 5, StORM overestimates the asymmetry of the rotational splitting in $l = 1$ multiplets of β Cep stars with a rotation frequency $f_{\rm rot}$ greater than 10% of the Keplerian critical rotation frequency $f_{\rm crit}$. This subsequently leads to the estimated $f_{\rm rot}$ being smaller than when extracting the $f_{\rm rot}$ from a simplified, a posteriori estimate based on the first-order rotation treatment of the GYRE oscillation code. When $f_{\rm rot} = 0$, StORM reproduces the frequencies computed with GYRE to within observational errors (Vanlaer et al. submitted). Consequently, by comparing the modelling results from these two codes, we essentially evaluate the impact of the second-order rotation effects. The most notable of these effects are the asymmetric rotational splitting and stellar deformation reducing mode frequencies.

In this appendix, we compare the modelling outcomes of different modelling methodologies in order to answer the following questions: a) does the reduction of mode frequencies due to stellar deformation and shifts in zonal frequency from mode coupling lead to a better match with the observed zonal frequencies; b) does our consistent inclusion of asymmetric rotational splitting in the χ^2 cost function worsen fitting of the other observations; c) how does the choice of oscillation code and modelling strategy affect the statistical stellar parameters estimates?

We repeated the modelling of our 36 stars using the same grid of stellar models, though with the oscillation computations performed with GYRE. Herein our modelling method was identical to the one described in Sect. 4 with two notable changes. Firstly, as zonal mode frequencies f_0 are unchanged by rotation to first order, the procedure of fixing the age of each evolutionary track using the fixed mode only needed to be performed for $f_{\rm rot} = 0$ rather than for each of the 41 $f_{\rm rot}$ in the StORM grid. Secondly, the optimal $f_{\rm rot}$ is determined from the observed rotational splitting $\Delta f = f_m - f_0$ with f_m the frequency of the multiplet's mode of azimuthal order m by calculating the Ledoux constant $C_{\rm nl,j}$ (Ledoux 1951) with GYRE and minimising $\sum_{\rm j}(\Delta f_{\rm obs,j} - m_{\rm j}(1 - C_{\rm nl,j})f_{\rm rot})^2/\sigma^2_{\Delta f_{\rm obs,j}}$. Since $f_{\rm rot}$ only affects non-zonal modes in a first-order treatment, interpolating zonal frequencies or stellar parameters in $f_{\rm rot}$ was not necessary. After the optimal model for each evolutionary track was determined, we again built a statistical model with an $\exp(-\chi^2/2)$ weighted average and computed the uncertainties on all parameters by demanding the uncertainty on M, $\log D_{\rm mix,0}$, and $f_{\rm ov}$ be at least half a grid step. Herein, the χ^2 cost function included $\log T_{\rm eff}$, $\log L$, the identified f_0, and the identified Δf. Next, we repeated both the analyses with the StORM and GYRE grid, but excluding Δf from the χ^2 cost function so the models are primarily optimised to the identified f_0. Herein the observed Δf were still used to optimise $f_{\rm rot}$ for each evolutionary track.

We first examine the impact of second-order rotation effects on the modelling of zonal modes by using the results found when neglecting the contributions of Δf to χ^2. Figure B.2 compares the largest discrepancy between the observed f_0 and the those in the model closest to the statistically selected parameters found with StORM and GYRE. Most stars lie well below the grey dotted line, indicating that the model found based on the StORM grid outperforms the GYRE model. Therefore, we conclude that the treatment of rotationally induced stellar deformation included in StORM improves the fitting of the observed f_0.

Next, Fig. B.3 compares the model quality with and without the contribution of Δf to χ^2 using the StORM grid. On one hand, the observed f_0 are better reproduced when the discrepancy in Δf is not minimised alongside f_0 in β Cep stars rotating more

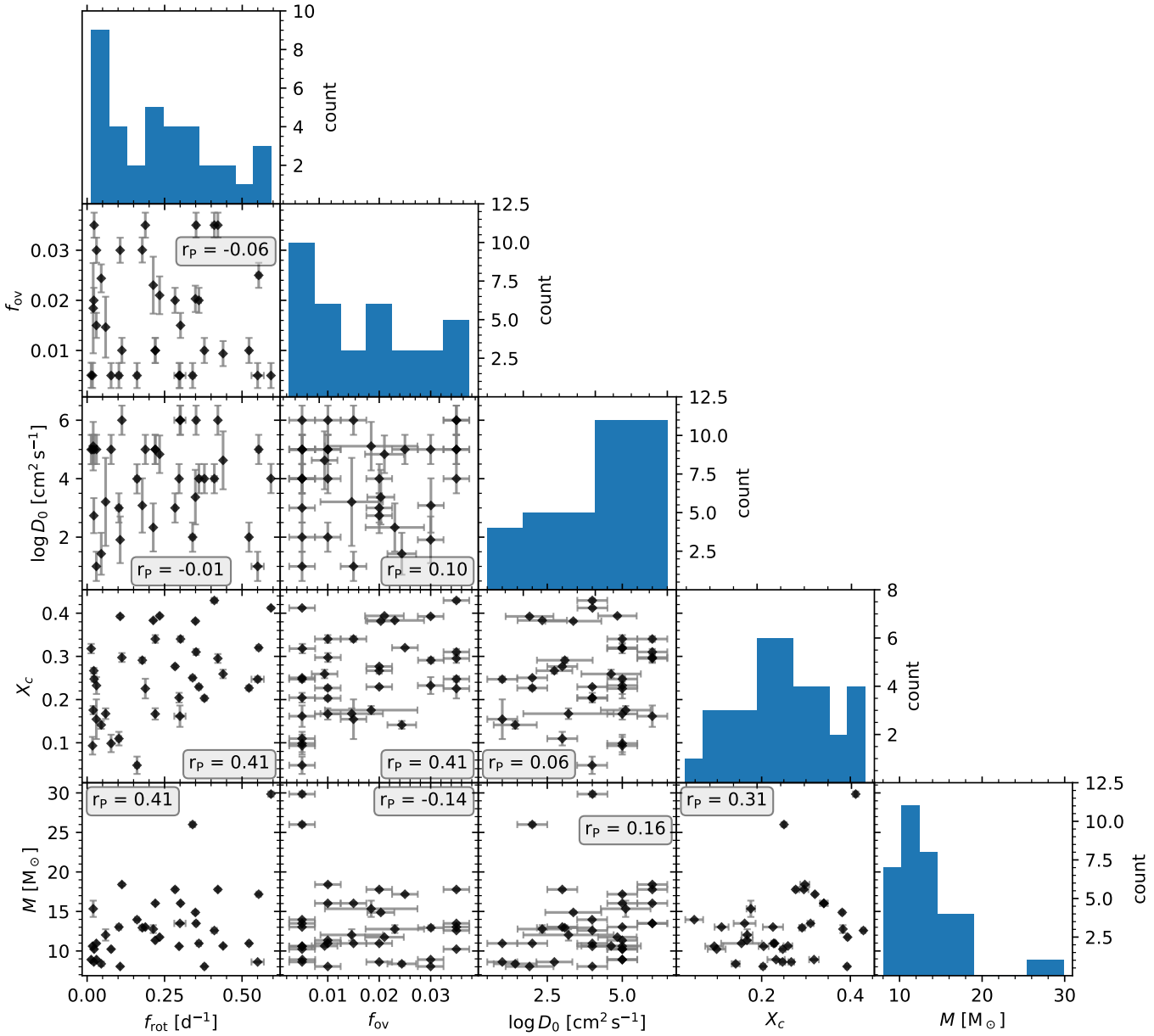

Fig. A.1: Corner plot of the rotation frequency, core overshoot parameter, envelope mixing strength, central hydrogen mass fraction and initial mass. Pearson correlation coefficients between each set of two parameters are included in boxes.

rapidly than 20% $f_{\rm crit}$. This indicates that beyond this rotation threshold, the difficulty in matching the observed rotational splitting may throw off the fitting of zonal frequencies. Figure B.4 shows two such stars, where one's best model is barely affected and the other's strongly affected by the change in cost function. On the other hand, the observed asymmetry parameter and the mean rotational splitting $\overline{\Delta f}$ are naturally better reproduced when Δf is included in the cost function. Notably, $\overline{\Delta f}$ is much better reproduced when including second-order effects at small $f_{\rm rot}/f_{\rm crit}$. These differences are exaggerated as $\overline{\Delta f}$ is reproduced highly precisely in both approaches, meaning the discrepancies in $\overline{\Delta f}$ are small, thus making the ratio volatile. Nevertheless, this demonstrates that optimising asymmetric rotational splitting from second-order effects is still worthwhile even when $f_{\rm rot}$ is small, as also argued by Briquet et al. (2007). In summary, the inclusion of Δf in χ^2 can adversely affect the fitting of f_0 when $f_{\rm rot} > 20\%\ f_{\rm crit}$ and thus potentially throw off stellar parameters such as mass and age. However, it also leads to significantly better reproduction of non-zonal frequencies and thus produces a superior $f_{\rm rot}$ estimate at all rotation rates. Consequently, whether Δf should be included in the cost function depends on which stellar parameters and thus which observables one prioritises, as well as the rotation regime.

To test how these different modelling approaches affect the derived stellar parameters, Fig. B.5 shows the five free parameters and the relative convective core mass $M_{\rm cc}/M$ obtained when including or excluding the Δf from χ^2. By and large, these modelling approaches produce similar results as the initial mass M and the central hydrogen mass fraction $X_{\rm c}$ as a proxy of age agree for most stars. Subsequently, $M_{\rm cc}/M$ is also in agreement. Nonetheless, there are a handful of stars for which the two modelling procedures differ significantly as a different local minimum in the cost function becomes the global minimum.

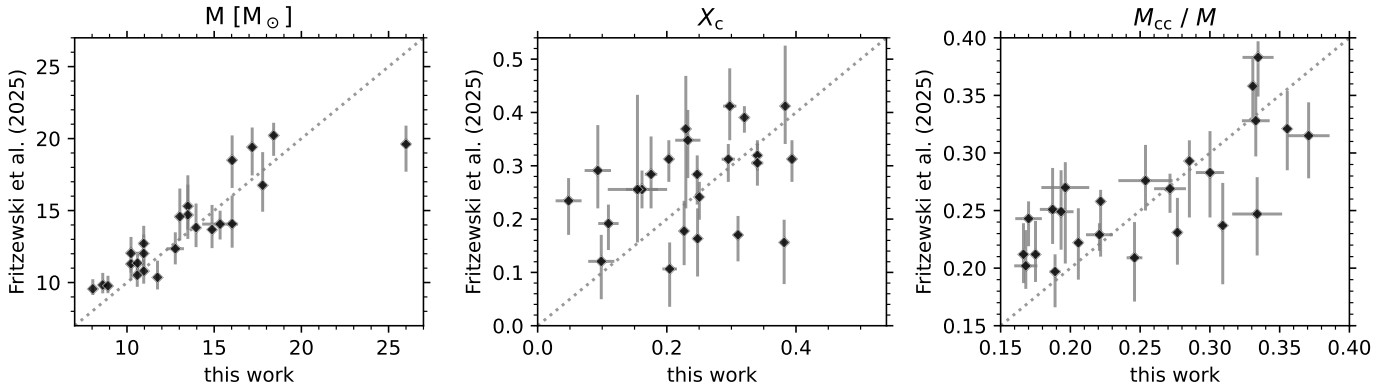

Fig. B.1: Comparison of the initial mass, central hydrogen mass fraction, and relative convective core mass from our modelling of 24 stars with the modelling by Fritzewski et al. (2025). The grey dotted lines indicate where the results from the two modelling procedures agree.

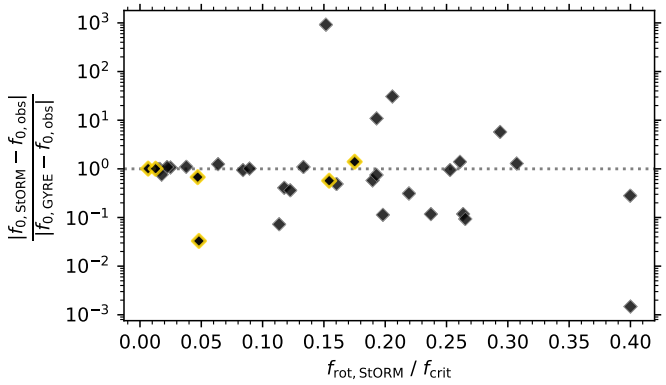

Fig. B.2: Ratio of the largest absolute difference between the observed and best model's zonal mode frequencies modelled with `StORM` over `GYRE` and neglecting rotational splitting in the optimisation against the relative rotation frequency. For stars below the grey dotted line, the modelling using `StORM` better reproduces the observed zonal modes than the modelling with `GYRE` and vice versa. The validation stars have a golden outline.

For completeness, we also compare the modelling results with `StORM` and `GYRE` in Fig. B.6 with Δf considered in χ^2. Again, most parameters are broadly in agreement, although X_c is underestimated when using `GYRE` for relatively rapidly rotating β Cep stars as the reduction of mode frequencies due to stellar deformation is neglected. This results in notable differences in the estimates of the other free parameters, larger than the scatter than in Fig. B.5. As also discussed in Sect. 5, the optimal f_{rot} is usually greater when using `GYRE` than when using `StORM`, especially at relatively high f_{rot}.

Appendix C: Sensitivity kernels

The low-radial order pulsations in β Cep stars typically have a broad rotational sensitivity kernel K_{nl}. Figure C.1 displays K_{nl}, calculated using equation (3.356) in Aerts et al. (2010) with the vertical and horizontal displacements computed by `StORM`, of the identified rotationally split multiplets in two stars. TIC 314833456 (top) has one multiplet sensitive to a thin region near the core and another sensitive to a broad part of the envelope, hence its core-to-envelope rotation ratio can be well con-

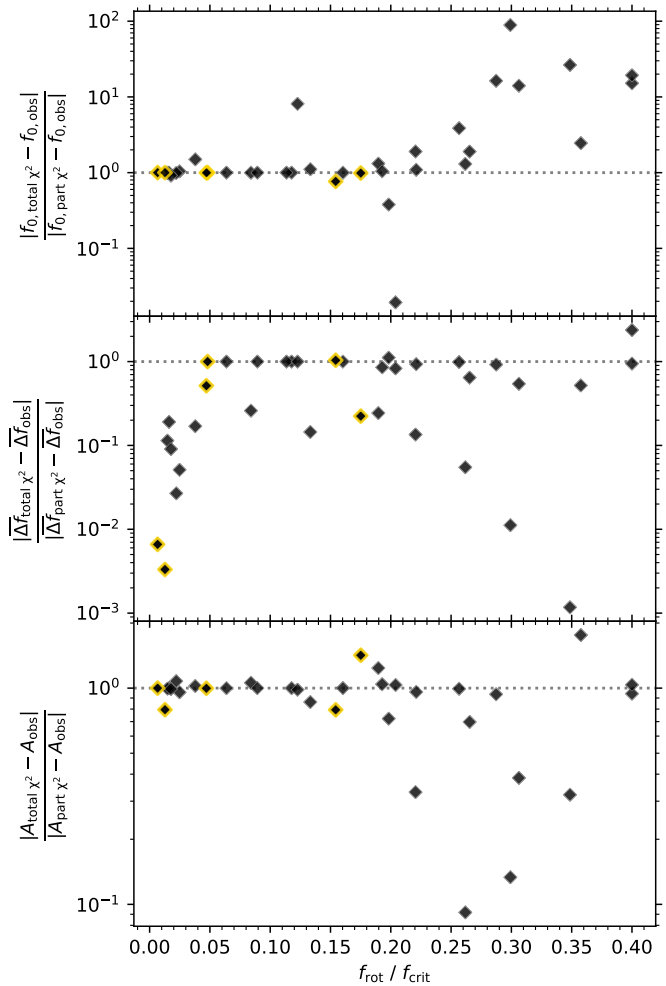

Fig. B.3: Ratio of the largest absolute difference between the observations and best model when including over excluding the rotational splitting from the cost function. The top panel shows the discrepancies in zonal mode frequencies, the middle panel the mean splitting within a multiplet, and the bottom panel the asymmetry. For stars below the grey dotted line, the modelling with rotational splitting in the cost function outperforms that without and vice versa. The validation stars have a golden outline.

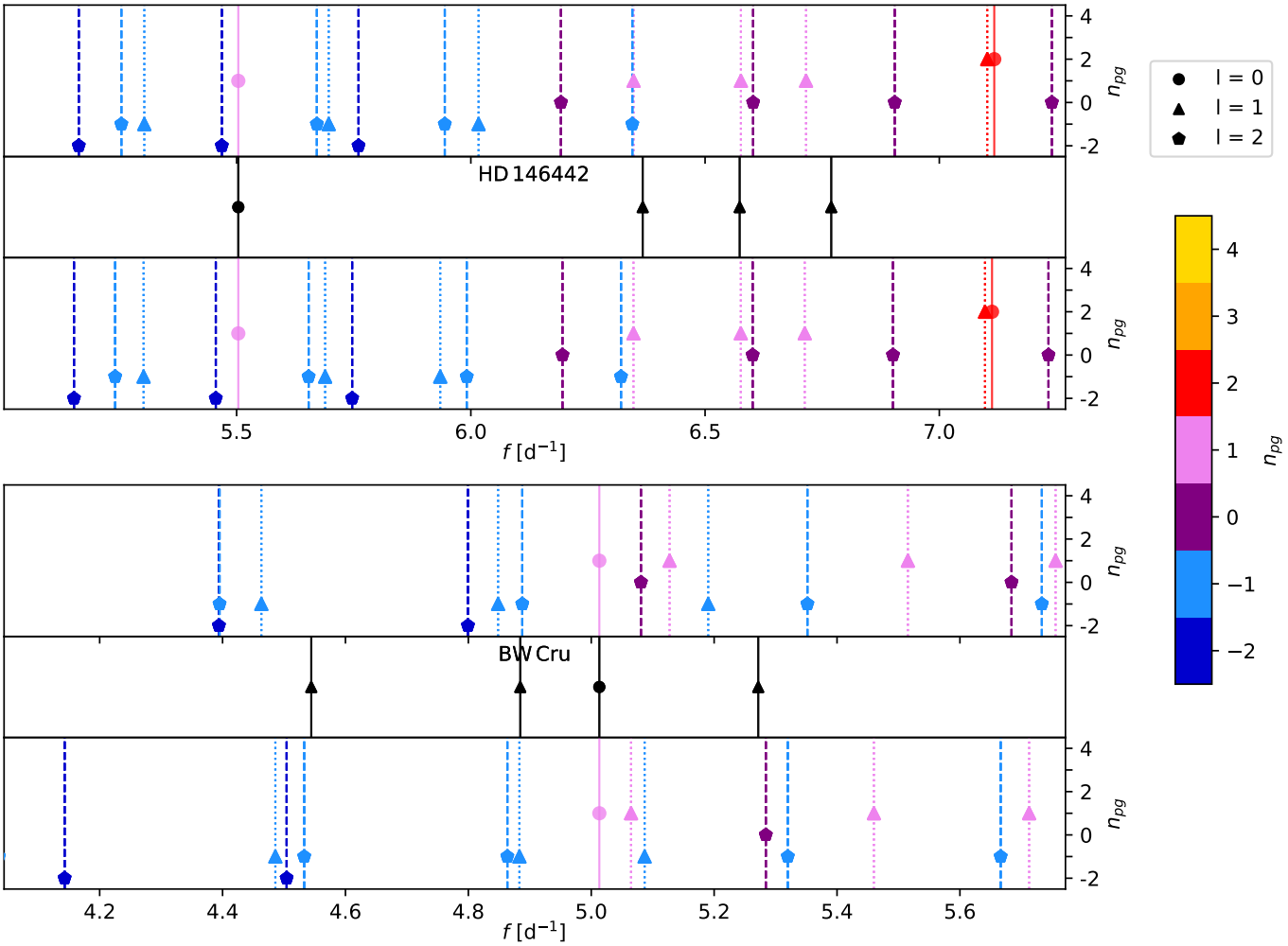

Fig. B.4: Idem Fig. 3, comparing two modelling approaches to observations for two examples. The three panels show the frequencies in the best model found with StORM when including rotational splitting in the χ^2 cost function (top), the observations – neglecting amplitude for clarity – (middle), and the best model found with StORM when excluding rotational splitting (bottom).

strained. Meanwhile, θ Oph has two multiplets that are both sensitive to approximately the same broad regions of the envelope. Consequently, these overlapping kernels average the rotation frequency over the same values, dampening the difference between the two measured rotation frequencies. Therefore, the constraint on the differential rotation in this star is merely a lower limit.

Appendix D: Electronic data and figures

This paper is accompanied by a number of electronic tables containing all the observational constraints as well as all the modelling results required to reproduce the figures presented in the main text. Snippets of these tables are shown in this Appendix.

The full Tables D.1, D.2, D.3, and D.4 are only available in electronic form at `https://github.com/Mathijs-Vanrespaille/Vanrespaille_BetaCepheiForwardModelling.git` (placeholder, to be replaced with CDS information). The `Python` code used to perform our forward modelling is available at `https://github.com/Mathijs-Vanrespaille/BCep_forward_modelling.git` (placeholder). The `MESA` stellar models, including the `StORM` oscillation computations, can be freely accessed at the KU Leuven Research Data Repository (link to be added). Meanwhile, the `MESA` work directory and `StORM` setup can be found at the following Zenodo repository (link to be added).

Electronic figures similar to Figs. 3 and C.1 for all 36 β Cep stars in our sample are available at the Zenodo repository (link to be added).

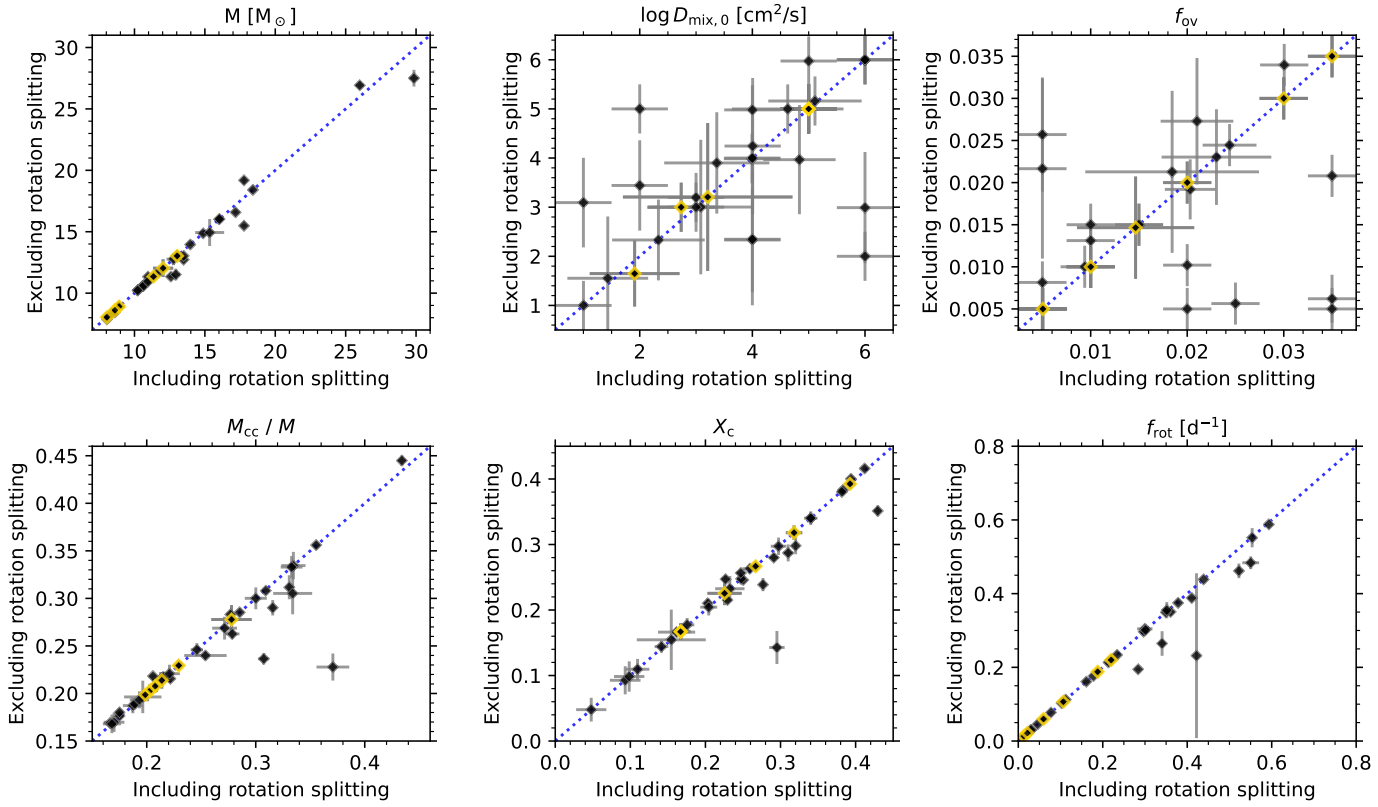

Fig. B.5: Comparison of the statistical estimates of initial mass, mixing at the base of the envelope, core overshoot parameter, relative convective core mass, central hydrogen mass fraction, and rotation frequency found with and without the rotational splitting in the χ^2 cost function. The validation stars have a golden outline. Grey dotted lines indicate where the modelling results agree.

Table D.1: Observational input of five stars examined in this study, including mode identifications. For simplicity, we omitted the uncertainties and the full lists of all detected signals in this excerpt. Similarly, we only show one identified signal for brevity.

TIC ID	Name	*Gaia* DR3 ID	RA [°]	dec. [°]	V [mag]	success	source $T_{\rm eff}$	$\log T_{\rm eff}$ [K]	$\log L$ [$L_\odot$]	G [mag]	A_G [mag]	d [pc]	$v \sin i$ [km s^{-1}]	$f_{\rm rot,surface} \sin i$ [d^{-1}]	$N_{\rm i}$	$N_{\rm f}$	i_1	$n_{pg,1}$	l_1	m_1	f_1 [d^{-1}]	a_1
13332837	HD 229085	2061190956100233216	305.39636	38.61325	9.8	True	ESP-HS	4.366	4.172	9.74	1.99	1672.2	180.8	0.48	2	5	1	2	1	-1	8.638539	0.001555
14085632	TIC 14085632	2057943789022547968	305.72188	37.11278	11.0	True	ESP-HS	4.533	4.938	10.67	3.49	2042.7	161.6	0.38	2	7	1	1	1	-1	4.521608	0.003241
15166556	HD 146442	5990434159009247232	244.59709	-45.84034	9.11	True	ESP-HS	4.362	3.727	8.98	1.49	900.2	177.0	0.76	2	4	1	1	1	-1	6.366871	0.002721
18827544	TIC 18827544	5941164183970835456	247.97767	-48.42875	12.28	False	ESP-HS	4.398	3.939	11.84	2.38	2602.8	96.5	0.38	2	4	1	…	1	-1	4.39127	0.000732
34590771	β CMa	…	95.67494	-17.95592	1.97	True	(1)	4.4	4.45	…	…	…	…	…	2	3	1	1	0	0	3.9995	2.6
…																						

Notes. $N_{\rm i}$ is the number of identified radial modes or rotationally split multiplets, i.e. how many unique $(n_{\rm pg}, l)$ are known, while $N_{\rm f}$ is the number of identified modes observed. The columns suffixed with $_1$ describe the first identified pulsation mode. The full table, including uncertainties, all identified frequencies, and lists of all detected frequencies including unidentified ones, is available at the CDS along with extra documentation.

References. (1) Mazumdar et al. (2006); (2) Briquet et al. (2007); (3) Aerts et al. (2003); (4) De Ridder et al. (2004); (5) Burssens et al. (2023).

Table D.2: Modelling outcomes and statistical parameter estimation of five stars examined in this study when modelled using `StORM` and including rotational splitting in the cost function. For simplicity, we omitted the uncertainties in this excerpt.

TIC ID	Name	χ^2	$\chi^2_{\rm reduced}$	$\lvert f_{0,obs} - f_{0,model} \rvert$ [d^{-1}]	M [$M_\odot$]	$\log D_{\rm mix,0}$ [cm^2 s]	$f_{\rm ov}$	$X_{\rm c}$	$f_{\rm rot}$ [d^{-1}]	$f_{\rm rot}/f_{\rm crit}$	age [yr]	$\log T_{\rm eff}$ [K]	$\log L$ [$L_\odot$]	$\log g$ [cm s^2]	$\log R$ [$R_\odot$]	$M_{\rm cc}$ [$M_\odot$]	$M_{\rm cc}/M$
13332837	HD 229085	59317.5	29658.7	0.000008	12.59	4.0	0.035	0.4294	0.41058	0.20392	10921648.3	4.43	4.268	3.946	0.796	3.8696	0.307
14085632	TIC 14085632	1268.7	317.2	0.006026	18.41	6.0	0.01	0.2974	0.11231	0.08403	7735004.7	4.477	4.798	3.765	0.968	6.1586	0.335
15166556	HD 146442	1844.8	1844.8	0.002667	8.04	4.0	0.01	0.2031	0.3785	0.22111	29556033.4	4.295	3.702	3.775	0.784	1.3377	0.166
34590771	β CMa	0.8	0.8	0.000049	12.03	3.2	0.0147	0.1674	0.05978	0.04806	15668112.5	4.37	4.306	3.644	0.936	2.5699	0.214
42940133	HD 228101	368.8	184.4	0.001323	11.75	4.8	0.021	0.3938	0.23399	0.11774	12556231.7	4.411	4.183	3.926	0.791	3.2514	0.277
…																	

Notes. The full table, including uncertainties, is available at the CDS along with extra documentation. Similar tables using the alternative modelling methods described in Appendix B.2 are also available at the CDS.

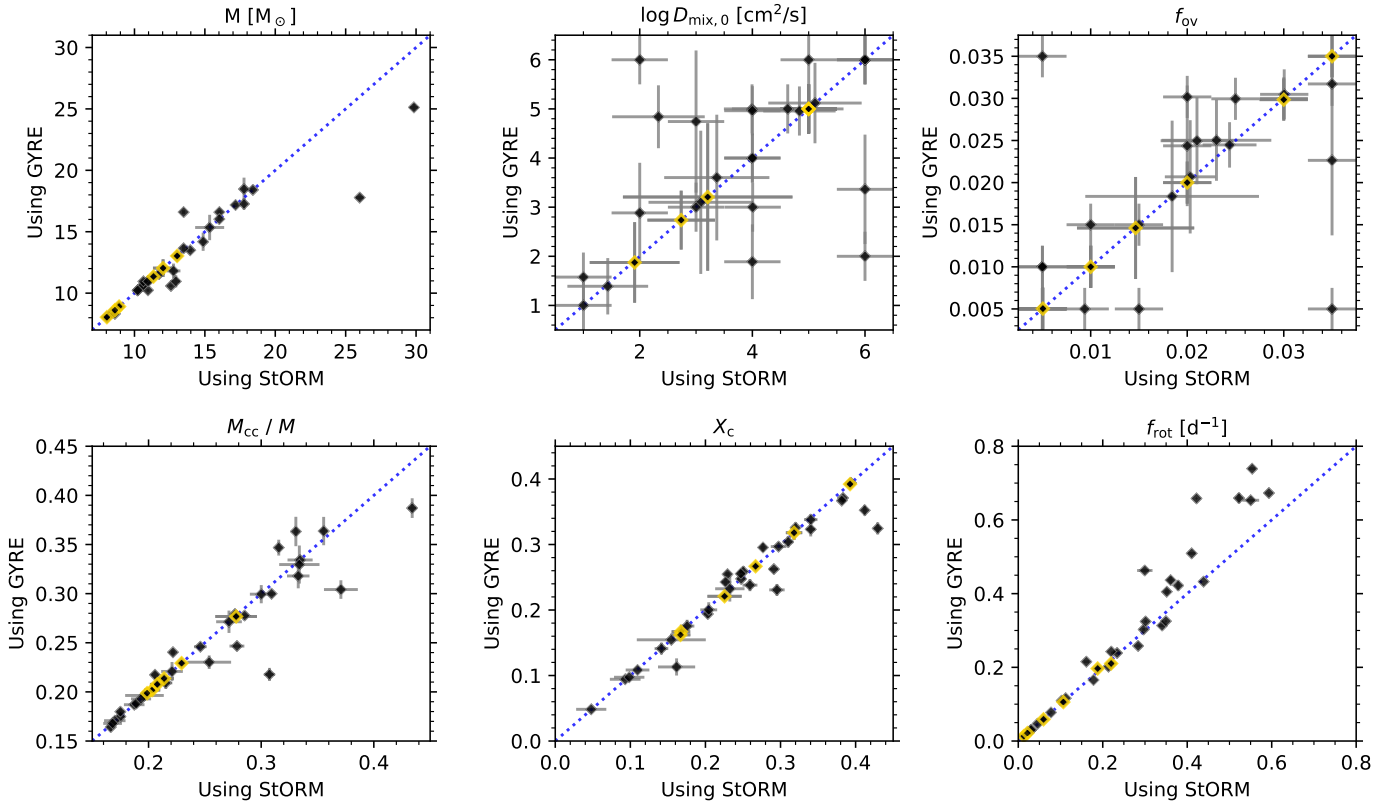

Fig. B.6: Comparison of the estimates of initial mass, mixing at the base of the envelope, core overshoot parameter, relative convective core mass, central hydrogen mass fraction, and rotation frequency using the `StORM` and `GYRE` grids. The validation stars have a golden outline. Grey dotted lines indicate where the modelling results agree.

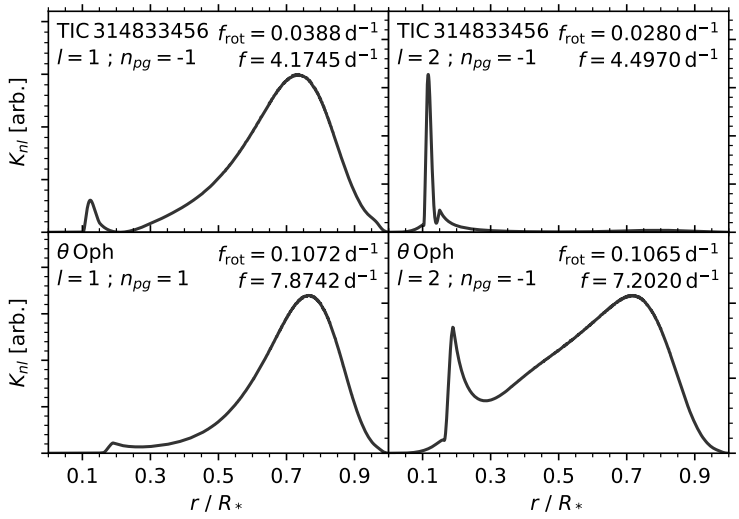

Fig. C.1. Sensitivity kernels of each identified rotationally split multiplet in the β Cep stars TIC 314833456 and θ Oph against the relative radius. In each panel, we include the name of the star and the multiplet's degree, radial order, zonal frequency, and extracted rotation frequency.

Table D.3: Observed and the best model's rotational splitting in each identified multiplet of five stars in our sample.

TIC ID	Name	$n_{\rm pg}$	l	$f_{0,\rm obs}$ [d^{-1}]	$f_{0,\rm model}$ [d^{-1}]	$\Delta f_{1,\rm obs}$ [d^{-1}]	$\Delta f_{-1,\rm obs}$ [d^{-1}]	$\Delta f_{2,\rm obs}$ [d^{-1}]	$\Delta f_{-2,\rm obs}$ [d^{-1}]	$A_{1,\rm obs}$	$A_{2,\rm obs}$	$\Delta f_{1,\rm model}$ [d^{-1}]	$\Delta f_{-1,\rm model}$ [d^{-1}]	$\Delta f_{2,\rm model}$ [d^{-1}]	$\Delta f_{-2,\rm model}$ [d^{-1}]	$A_{1,\rm model}$	$A_{2,\rm model}$	$f_{\rm rot}$ [d^{-1}]	$\sigma_{f_{\rm rot}}$ [d^{-1}]	$f_{\rm rot,GYRE}$ [d^{-1}]	C_{nl}
13332837	HD 229085	2	1	9.131843	9.131843	0.591194	0.493303	…	…	-0.090264	…	0.254634	0.555308	…	…	0.371229	…	0.41735	0.00069	0.56559	0.04127
13332837	HD 229085	1	1	6.877143	6.877151	…	0.386102	…	…	…	…	0.266755	0.386142	…	…	0.182858	…	0.38376	0.02898	0.40202	0.03959
14085632	TIC 14085632	1	1	4.633045	4.633045	0.138601	0.111438	…	…	-0.108636	…	0.107998	0.131965	…	…	0.099877	…	0.12751	0.00086	0.13301	0.06005
14085632	TIC 14085632	-1	2	4.216509	4.210483	0.09717	0.073407	…	0.159607	-0.139309	…	0.07823	0.080656	0.153429	0.164785	0.015266	0.035685	0.10474	0.0007	0.11286	0.24158
15166556	HD 146442	1	1	6.57384	6.576507	0.195471	0.206969	…	…	0.028572	…	0.139057	0.229058	…	…	0.244492	…	0.3785	0.0045	0.41645	0.51682
15166556	HD 146442	1	0	5.503586	5.503586	…	…	…	…	…	…	…	…	…	…	…	…	…	…	…	…
34590771	β CMa	1	0	3.9995	3.9995	…	…	…	…	…	…	…	…	…	…	…	…	…	…	…	…
34590771	β CMa	-2	2	3.8828	3.882751	…	…	0.0965	…	…	…	0.048612	0.049342	0.096497	0.099494	0.007457	0.015292	0.05978	0.00164	0.05889	0.18062
42940133	HD 228101	0	2	7.167395	7.166072	0.222594	0.242747	…	0.435669	0.043309	…	0.214158	0.221395	0.420891	0.449875	0.016617	0.033285	0.23401	0.00229	0.23495	0.0661
42940133	HD 228101	1	0	6.302448	6.302448	…	…	…	…	…	…	…	…	…	…	…	…	…	…	…	…
…																					

Notes. Note that each row in this table represents one rotationally split multiplet or radial mode, meaning there are several rows per star. We included the statistical rotation frequency estimate from our modelling, its uncertainty, and the rotation frequency found with the simplified a posteriori step using `GYRE` and the corresponding Ledoux constant. In the subscripts of rotational splitting $\Delta f_{m,\rm source}$ and asymmetry $A_{|m|,\rm source}$, 'm' indicates the azimuthal order and 'source' whether the value comes from the observations or the best model. The zonal frequencies $f_{0,\rm source}$ use the same scheme. The full table is available at the CDS along with extra documentation.

Table D.4: The constraints on differential rotation in five stars in our sample. We only show the rotation and kernel positions from one rotationally split multiplet for brevity.

TIC ID	Name	$f_{\rm rot,surface}\sin i$	$\sigma_{f_{\rm rot,surface}\sin i}$	$f_{\rm rot}$	$\sigma_{f_{\rm rot}}$	$X_{\rm c}$	$\sigma_{X_{\rm c}}$	$N_{\rm r}$	$f_{0,1}$	n_1	l_1	$f_{\rm rot,1}$	$\sigma_{f_{\rm rot,1}}$	$(r/R_*)_{\rm mode,1}$	$(r/R_*)_{\rm mean,1}$	$(r/R_*)_{\rm median,1}$
13332837	HD 229085	0.48	0.15	0.41058	0.00817	0.4294	0.0045	2	9.131843	2	1	0.41735	0.00069	0.882	0.7384	0.8373
14085632	TIC 14085632	0.38	0.1	0.11231	0.00088	0.2974	0.0104	2	4.633045	1	1	0.12751	0.00086	0.7436	0.4308	0.4371
15166556	HD 146442	0.76	0.23	0.3785	0.0045	0.2031	0.005	1	6.57384	1	1	0.3785	0.0045	0.1315	0.4506	0.1956
34590771	β CMa	…	…	0.05978	0.00164	0.1674	0.0124	1	3.8828	-2	2	0.05978	0.00164	0.1235	0.4058	0.3842
42940133	HD 228101	0.46	0.12	0.23399	0.00231	0.3938	0.0028	1	7.167395	0	2	0.23401	0.00229	0.205	0.4051	0.2648
…																

Notes. N_r is the number of identified rotationally split multiplet. The columns $(r/R_*)_{\rm X}$ are the relative radius of the position of the maximum, mean and median of the sensitivity kernel K_{nl}. The columns suffixed with $_1$ describe the first identified multiplet. The full table, including all identified rotationally split multiplets, is available at the CDS along with extra documentation.